Continuum Mech. Thermodyn. (2020) 32:621–645
https://doi.org/10.1007/s00161-018-0701-3

ORIGINAL ARTICLE

M. Cuomo · L. Greco

An implicit strong G^1-conforming formulation for the analysis of the Kirchhoff plate model

Received: 3 May 2018 / Accepted: 19 July 2018 / Published online: 7 August 2018

Abstract In this work, we present a quadrilateral plate element for the Kirchhoff plate bending model that satisfies the continuity requirements in implicit way. The element is designed on the basis of the rational Gregory's enhancement of the bi-cubic Coons patch. This Coons-Gregory patch is based on the boundary data set of a surface, that accounts for both the displacement and the edge rotation along the sides of the element. In this way, an implicitly conforming interpolation with 20-dofs per element is obtained. The Coons-Gregory patch ensures G^1-conformity only for the case of structured meshes. Numerical examples show that the proposed formulation is highly efficient with respect to accuracy, rate of convergence and robustness.

Keywords Conforming plate element · Kirchhoff plate model · Gregory's patch · G^1 continuity

1 Introduction

1.1 Motivation of the work

The development of efficient finite elements for thin plates and shells is still an active field of research in computational mechanics and engineering applications. One of the main issues with finite elements discretization of plates and shells is the geometrical continuity of the normal across elements in any configuration. Many formulations have been proposed and are currently adopted for plates, as will be briefly reviewed in the following sections. Recently, a strong emphasis has been given to develop plate and shell models based on isogeometric analysis (IGA) that, employing B-spline (and NURBS) representations with high degree of continuity, allows to meet the requirements for the slope across adjacent elements [1].

Most of the numerical formulations use independent interpolations for displacements and rotations, according to Mindlin's plate theory. Displacement formulations, whose kinematics according to Kirchhoff's theory is defined by one field only, the displacement of the middle plane, are less common, but have the advantage that are free of the shear locking, so they can be safely used also for very thin plates. Furthermore, lower computational efforts are needed with respect to the numerical formulation based on displacements and rotations. Numerical formulation for Kirchhoff's plates requires C^1-continuity for the displacement field. Finite element formulations that exactly fulfill the continuity requirement along the element sides are known as conforming formulations. The continuity requirement implies that there exists a unique tangent plane to the deformed

Communicated by Francesco dell'Isola.

M. Cuomo (✉) · L. Greco
Dipartimento di Ingegneria Civile e Architettura (DICAR), Universitá degli Studi di Catania, Via Santa Sofia 54, 95125 Catania, Italy
E-mail: mcuomo@dica.unict.it
E-mail: leopoldo.greco@virgilio.it

configuration at any point along the element boundaries, a condition known as geometric G^1-continuity (the exact definition of G^1-continuity will be discussed in Sect. 3).

Strongly conforming Kirchhoff plate elements are more efficient form the computational point of view and allow in a simple way the coupling with high order elements like beams. In this work, we develop a conforming formulation for Kirchhoff's plate, which implicitly satisfies G^1-continuity at any point. Since this condition is independent on the parametrization adopted for the element, we formulate the element directly in absolute coordinates, through a map from the intrinsic coordinates, rather than using parent elements as commonly done in FEM.

Conforming interpolations for the plate bending problem have long been investigated. The construction of a C^1-conforming space can be very difficult for general patch geometries, for a complete overview see [2]. Among the oldest formulations, the complete compatible bi-cubic BFS-interpolation, proposed by Bogner,Fox and Schmit in [3], results in a conforming element for regular quadrilateral meshes. The ACM-element (Adini-Clough-Melosh) without twisting degrees of freedom, on the contrary does not respect conformity. De Veubeke succeeded in building a conforming element for general quadrilateral mesh decomposing the quadrilateral in four triangular sub-elements and combining the displacement interpolations [4]. In [5], the suitability of the BFS-interpolation on the C^1-conforming meshes is shown. Other kinds of conforming elements can be obtained including additional degrees of freedom (the higher derivatives of the displacement), as done in [6] for the triangular and quadrilateral case. In [7], the quintic triangular Argyris' element is adopted for second gradient numerical applications. In [8], many conforming elements are discussed in the framework of the second gradient elasticity.

In the framework of the Kirchhoff model, the continuity conditions for the boundary of the element can be relaxed in a weak sense, or alternatively the Kirchhoff constraint can be collocated obtaining a discrete version of the conformity condition. The latter class of elements is known as Discrete Kirchhoff constrained elements. The Kirchhoff constraint is imposed at a discrete number of points, (generally the integration points of the edges), obtaining a linear set of equations, that solved allows the reduction of the degrees of freedom, see [9–12]. Analogous to this idea is the formulation of the semi-Loof elements, see [13]. A triangular element having the normal derivative of the displacement along the edges as degree of freedom was first introduced by Clough and Tocher (HCT element) [14]. The latter class of elements have proved to be very effective in convergence rate and accuracy, but their combination with other elements is in general difficult.

Although not the subject of this paper, it is useful to recall that the difficulties related to the continuity requirements are relaxed using elements based on the *Reissner-Mindlin* theory, since only a C^0-continuity for the kinematic fields is needed, but the finite element can suffer of shear locking in the thin limit. Mixed strategies can be adopted to obtain locking free formulations, among the oldest those proposed by de Veubeke and Herrmann [15,16]. Many other elements have been proposed since (see for instance [17–19]; within this context, Bathe developed the Assumed Natural Strain Formulation in the MITC family of elements [20]. The elements were extensively analyzed in [21,22]. The MITC elements at the moment probably constitute the reference Finite Elements for shells and plates see [23], at least for what concerns quadrilateral elements. For this reason in the numerical examples, we will compare the performance of the proposed element with the results obtained with plate MITC elements.

1.2 Objectives of the work

In this work, we discuss a finite element, based on a rational approximant, that implicitly accounts for strong G^1-continuity. A quadrilateral element employing a modified bi-Hermitian interpolation is developed.

The proposed G^1-conforming formulation is based on the rational Coons-Gregory approximant on the quadrilateral element of a structured mesh. An overlook to this methodology for CAD can be found in [24]. The idea consists in introducing an ad hoc parametrization of the edge tangent manifold called the ribbon, see [24,25], that has the same configuration space of a Kirchhoff rod, see [26–29]. It will be shown that this approach in the case of cubic interpolation consists in a particular generalization of the bi-Hermitian interpolation in which the twist degrees of freedom are substituted by two independent edge rotations.

A quadrilateral conforming finite element with 20-dofs is obtained, in which the basis functions are enhanced with rational combinations. This introduces discontinuity on the second derivatives that do not have an unique value at the corners. In the case of structured meshes of quadrilateral elements, the element will be shown to present good properties of accuracy and rate of convergence, comparable to the most efficient elements used in FE analysis. The moments also are accurate, and the indeterminacies at the corners can be overcome by means of stress recovery strategies, like those described in [30,31]. The presentation of this paper is restricted to meshes that have a G^1-continuous parametrization (i.e., structured meshes).

The outline of the paper is as follows. In Sect. 2, the basic equations of Kirchhoff plates are briefly revised, then in Sect. 3 the newly proposed element is described in details. Finally, some examples will be discussed, in order to investigate the performance of the element.

2 The Kirchhoff plate problem

Let us consider a plate whose middle plane is defined in an open set $\Omega \subset \mathbb{R}^2$, with a piecewise continuous boundary $\partial\Omega = \bigcup_i \partial\Omega_i$, and corners $\partial\partial\Omega_i$. We shall assume that the region Ω is simply connected, and homeomorphic to a rectangle. Indeed, since in this work, we develop only quadrilateral elements, it can be assumed that the region Ω can be subdivided in simply connected non overlapping domains Ω_i, each one continuously mapped from the parametric domain $\Lambda = (0, 1) \times (0, 1)$ and $\{\theta^1, \theta^2\} \in \Lambda$, such that the map is continuous everywhere without singularity points. In this way for each region Ω_i, four corners are present on the boundary. Let h be the thickness of the plate, $\zeta \in [-h/2, h/2]$, and $\hat{\boldsymbol{n}}$ be the unit normal vector to the middle plane of the plate. The position of a point of the plate is given by

$$\overset{*}{\boldsymbol{p}}(\theta^1, \theta^2, \zeta) = \boldsymbol{p}(\theta^1, \theta^2) + \zeta\, \hat{\boldsymbol{n}}. \tag{1}$$

Adopting the intrinsic formulation, see for instance [32,33], the geometry of the middle plane of the plate is characterized by the covariant tangent vectors defined as $\boldsymbol{t}_\alpha = \frac{\partial \boldsymbol{p}}{\partial \theta^\alpha}$ and by the covariant metric tensor $g_{\alpha\beta} = \boldsymbol{t}_\alpha \cdot \boldsymbol{t}_\beta$. The contravariant basis vectors are given by $\boldsymbol{t}^\alpha = g^{\alpha\beta}\boldsymbol{t}_\beta$.

2.1 Kinematics

In this paper, we analyze Kirchhoff plates. The equilibrium equations will be derived according to the classical treatment presented by Green [32]. The Kirchhoff hypotheses require that, during the deformation process, the following constraints be satisfied:

$$\hat{\boldsymbol{n}} \cdot \boldsymbol{t}_\alpha = 0 \quad \alpha = 1, 2, \quad \hat{\boldsymbol{n}} \cdot \hat{\boldsymbol{n}} = 1. \tag{2}$$

Using a superposed dot for indicating velocities, the tangent version of these constraints states that

$$\dot{\hat{\boldsymbol{n}}} \cdot \boldsymbol{t}_\alpha = -\left(\hat{\boldsymbol{n}} \cdot \frac{\partial \dot{\boldsymbol{p}}}{\partial \theta^\alpha}\right) \quad \alpha = 1, 2, \quad \dot{\hat{\boldsymbol{n}}} \cdot \hat{\boldsymbol{n}} = 0. \tag{3}$$

Small deformation and displacements are considered in this work, so that denoting by $w : \Omega \to \mathbb{R}$ the normal component of the displacement of the middle plane and by $\boldsymbol{\phi}$ the rotation vector of the unit normal, the displacement $\mathbf{u}$ of a generic point of the plate is given by

$$\mathbf{u}(\theta^1, \theta^2, \zeta) = w(\theta^1, \theta^2)\, \hat{\boldsymbol{n}} + \zeta\, \boldsymbol{\phi}(\theta^1, \theta^2) \times \hat{\boldsymbol{n}}. \tag{4}$$

Under the Kirchhoff hypotheses, the rotation vector becomes then

$$\boldsymbol{\phi} \times \hat{\boldsymbol{n}} \cdot \mathbf{t}_\alpha = -\hat{\boldsymbol{n}} \cdot \frac{\partial \mathbf{u}}{\partial \theta^\alpha} = -\frac{\partial w}{\partial \theta^\alpha}. \tag{5}$$

2.1.1 Bending curvatures

The curvature of the plate in the hypothesis of infinitesimal deformation, according to the Kirchhoff constraint (5) is given by:

$$\boldsymbol{\chi} = -\hat{\boldsymbol{n}} \cdot \left[\left(\frac{\partial^2 \mathbf{u}}{\partial \theta^\beta \partial \theta^\alpha} \right) \otimes \boldsymbol{t}^\alpha \otimes \boldsymbol{t}^\beta \right], \tag{6}$$

or, in components,

$$\begin{aligned} \boldsymbol{\chi} &= \chi_{\alpha\beta}\, \boldsymbol{t}^\alpha \otimes \boldsymbol{t}^\beta \\ &= -\left[\frac{\partial}{\partial \theta^\beta} \left(\frac{\partial w}{\partial \theta^\alpha} \right) - \frac{\partial w}{\partial \theta^\rho} \Gamma^\rho_{\alpha\beta} \right] \boldsymbol{t}^\alpha \otimes \boldsymbol{t}^\beta, \quad \Gamma^\rho_{\alpha\beta} = \left(\frac{\partial \boldsymbol{t}_\alpha}{\partial \theta^\beta} \cdot \boldsymbol{t}^\rho \right), \end{aligned} \tag{7}$$

that is, the curvature tensor is given by the second covariant derivative of the scalar function $w(\theta^1, \theta^2)$. The strain tensor is thus $\mathbf{E} = \zeta\, \boldsymbol{\chi}$.

2.2 Weak formulation

The virtual power identity for the plate is given by

$$\int_{-h/2}^{h/2} \int_\Omega \boldsymbol{\sigma} : \zeta\, \dot{\boldsymbol{\chi}}\, \mathrm{d}\Omega\, \mathrm{d}\zeta = \int_{-h/2}^{h/2} \int_\Omega b_z \dot{w} \mathrm{d}\Omega\, \mathrm{d}\zeta \tag{8}$$

for any virtual velocity field $\dot{w}$ and compatible velocity of curvature $\dot{\boldsymbol{\chi}}$ given by (7). In the external power, only body forces have been considered for brevity. Performing the double contraction, and introducing the moment resultants

$$M^{\alpha\beta} = \int_{-h/2}^{+h/2} \zeta\, \sigma^{\alpha\beta}\, \mathrm{d}\zeta, \tag{9}$$

the internal power reduces to

$$\Pi_{int} = \int_\Omega M^{\alpha\beta} \dot{\chi}_{\alpha\beta} \mathrm{d}\Omega = \int_\Omega \left(M^{11} \dot{\chi}_{11} + 2M^{12} \dot{\chi}_{12} + M^{22} \dot{\chi}_{22} \right) \mathrm{d}\Omega. \tag{10}$$

Considering a linear elastic isotropic constitutive behavior and the plane stress approximation valid for thin plates, the constitutive equations for the moment components become (see [32])

$$\begin{aligned} M^{\alpha\beta} &= \mathbb{C}^{\alpha\beta\mu\rho}\, \chi_{\mu\rho}, \\ \mathbb{C}^{\alpha\beta\mu\rho} &= \frac{E}{2(1+\nu)} \left(g^{\alpha\mu} g^{\beta\rho} + g^{\alpha\rho} g^{\beta\mu} + \frac{2\,\nu}{1-\nu} g^{\alpha\beta} g^{\mu\rho} \right). \end{aligned} \tag{11}$$

In the numerical formulation, the physical representation of all geometrical objects is considered. In physical components, the constitutive equations particularize to

$$\begin{gathered} M^{xx} = \mathrm{D} \left(\chi_{xx} + \nu \chi_{yy} \right), \quad M^{yy} = \mathrm{D} \left(\chi_{yy} + \nu \chi_{xx} \right), \quad M^{xy} = (1-\nu) \mathrm{D} \chi_{xy}, \\ \mathrm{D} = \frac{\mathrm{E} h^3}{12(1-\nu^2)}, \end{gathered} \tag{12}$$

so that the internal virtual power for the plate model reduces to

$$\Pi_{int} = \mathrm{D} \int_\Omega \left[\chi_{xx} \dot{\chi}_{xx} + \nu \left(\chi_{xx} \dot{\chi}_{yy} + \dot{\chi}_{xx} \chi_{yy} \right) + \chi_{yy} \dot{\chi}_{yy} + 2(1-\nu) \chi_{xy} \dot{\chi}_{xy} \right] \mathrm{d}\Omega. \tag{13}$$

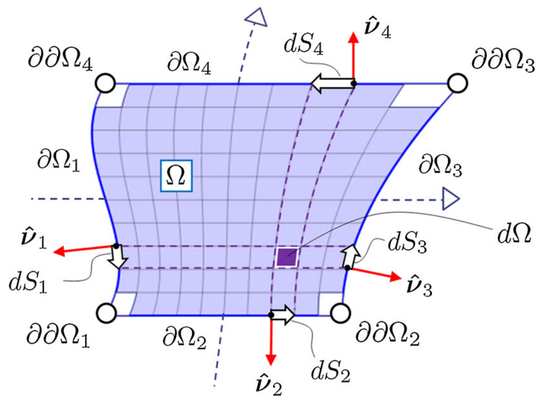

Fig. 1 Geometry definitions

2.2.1 Strong formulation

Let $\mathrm{d}\Lambda = \mathrm{d}\theta^1\mathrm{d}\theta^2$ be the element of area of the parametric space and $\sqrt{g} = \det[g_{\alpha\beta}]$. The physical element of area is $\mathrm{d}\Omega = \sqrt{g}\mathrm{d}\Lambda$. Introducing the definition (7) of the curvature tensor in the Eq. (10) and applying the *Green–Gauss–Ostrogradsky* formula, the internal virtual power becomes

$$\begin{aligned}\Pi_{int} = &\int_\Lambda \left(\frac{\partial}{\partial\theta^\beta}\left(\sqrt{g}M^{\rho\beta}\right) + \sqrt{g}M^{\alpha\beta}\Gamma^{\rho}_{\alpha\beta}\right)\frac{\mathrm{d}\dot{w}}{\partial\theta^\rho}\,\mathrm{d}\Lambda \\ &- \int_{\partial\Omega} M^{\alpha\beta}\frac{\partial\dot{w}}{\partial\theta^\alpha}\left(\boldsymbol{t}_\beta\cdot\hat{\boldsymbol{\nu}}\right)\mathrm{d}S.\end{aligned} \tag{14}$$

where $\hat{\boldsymbol{\nu}}$ is the outgoing unit normal to the boundary of the plate (see Fig. 1). Since $\frac{\partial\sqrt{g}}{\partial\theta^\beta} = \sqrt{g}(\Gamma^1_{1\beta} + \Gamma^2_{2\beta}) = \sqrt{g}\,\Gamma^\mu_{\mu\beta}$ the equation (14) reduces to

$$\Pi_{int} = \int_\Lambda \left(M^{\rho\beta}{}_{|\beta}\frac{\partial\dot{w}}{\partial\theta^\rho}\right)\sqrt{g}\,\mathrm{d}\Lambda - \sum_i\int_{\partial\Omega_i} M^{\alpha\beta}\frac{\partial\dot{w}}{\partial\theta^\alpha}\left(\boldsymbol{t}_\beta\cdot\hat{\boldsymbol{\nu}}_i\right)\mathrm{d}S_i \tag{15}$$

where the summation extends to the four sides of the boundary, and the term $M^{\rho\beta}{}_{|\beta}$ represents the contravariant components of the divergence of the bending moment tensor, $\boldsymbol{M} = M^{\alpha\beta}\boldsymbol{t}_\alpha\otimes\boldsymbol{t}_\beta$, defined as

$$M^{\rho\beta}{}_{|\beta} = \frac{\partial M^{\rho\beta}}{\partial\theta^\beta} + M^{\mu\beta}\,\Gamma^\rho_{\mu\beta} + M^{\rho\mu}\,\Gamma^\beta_{\mu\beta}. \tag{16}$$

First, we focus on the treatment of the boundary term of the Eq. (15). On each side of the boundary, a local system of normal and tangent coordinates ν, s is considered, with s arc length. Notice that the outgoing unit normal $\hat{\boldsymbol{\nu}}$ is given by the unit contravariant vectors

$$\begin{aligned}\hat{\boldsymbol{\nu}}_1 &= -\left.\frac{\mathbf{t}^1}{\|\mathbf{t}^1\|}\right|_{(0,\theta^2)} & \hat{\boldsymbol{\nu}}_3 &= \left.\frac{\mathbf{t}^1}{\|\mathbf{t}^1\|}\right|_{(1,\theta^2)} \\ \hat{\boldsymbol{\nu}}_2 &= -\left.\frac{\mathbf{t}^2}{\|\mathbf{t}^2\|}\right|_{(\theta^1,0)} & \hat{\boldsymbol{\nu}}_4 &= \left.\frac{\mathbf{t}^2}{\|\mathbf{t}^2\|}\right|_{(\theta^1,1)}\end{aligned} \tag{17}$$

Introducing the moment $\mathbf{M}^\nu = M^{\alpha\beta}(\mathbf{t}_\beta\cdot\hat{\boldsymbol{\nu}})\mathbf{t}_\alpha$ acting on the boundary of the plate, it is recognized that the boundary term of the Eq. (15) is given by the dot product between $\mathbf{M}^\nu$ and the gradient of the vertical velocity,

$$\begin{aligned}-\int_{\partial\Omega_i} M^{\alpha\beta}\frac{\partial\dot{w}}{\partial\theta^\alpha}\left(\boldsymbol{t}_\beta\cdot\hat{\boldsymbol{\nu}}_i\right)\mathrm{d}S_i &= -\int_{\partial\Omega_i}\mathbf{M}^\nu\cdot\nabla\dot{w}\,\mathrm{d}S_i \\ &= \int_{\partial\Omega_i} M^{s\nu}\left(-\frac{\partial\dot{w}}{\partial s}\right)\mathrm{d}S_i + \int_{\partial\Omega_i} M^{\nu\nu}\left(-\frac{\partial\dot{w}}{\partial\nu}\right)\mathrm{d}S_i,\end{aligned} \tag{18}$$

with $M^{s\nu} = M^{\alpha\beta}(\mathbf{t}_\beta \cdot \hat{\boldsymbol{\nu}})(\mathbf{t}_\alpha \cdot \hat{\mathbf{s}})$, $M^{\nu\nu} = M^{\alpha\beta}(\mathbf{t}_\beta \cdot \hat{\boldsymbol{\nu}})(\mathbf{t}_\alpha \cdot \hat{\boldsymbol{\nu}})$. The first term of the right-hand side of equation (18), following Kirchhoff's calculations, can be newly integrated by part along the edge curve, while the second term in the right-hand side represents the work done by the edge bending moment $M^{\nu\nu}$ for the edge rotation field along side i, $\dot{\phi}_i = -\left.\frac{\partial \dot{w}}{\partial \nu}\right|_i = -\left.\frac{\partial \dot{w}}{\partial \theta^\alpha}\mathbf{t}_\alpha \cdot \hat{\boldsymbol{\nu}}\right|_i$.

The Kirchhoff's boundary term gets the final form

$$-\int_{\partial\Omega_i} M^{\alpha\beta} \frac{\partial \dot{w}}{\partial \theta^\alpha} (\boldsymbol{t}_\beta \cdot \hat{\boldsymbol{\nu}}_i)\, \mathrm{d}S_i = \int_{\partial\Omega_i} \frac{\partial M^{s\nu}}{\partial s} \dot{w}_i\, \mathrm{d}S_i - \left[M^{s\nu}\dot{w}_i\right]_0^{L_i} + \int_{\partial\Omega_i} M^{\nu\nu}\dot{\phi}_i\, \mathrm{d}S_i. \tag{19}$$

The field integral is elaborated by a further application of the *Green–Gauss–Ostrogradsky* formula yielding

$$\int_\Lambda \left(\sqrt{g} M^{\rho\beta}{}_{|\beta}\right) \frac{\partial \dot{w}}{\partial \theta^\rho}\, \mathrm{d}\Lambda = -\int_\Lambda M^{\rho\beta}{}_{|\rho\beta}\, \dot{w}\, \sqrt{g} \mathrm{d}\Lambda + \int_{\partial\Omega_i} T_i^\nu\, \dot{w}_i\, \mathrm{d}S_i, \tag{20}$$

where $T_i^\nu = \mathrm{div}[\mathbf{M}] \cdot \hat{\boldsymbol{\nu}}_i = M^{\rho\beta}{}_{|\beta}(\boldsymbol{t}_\rho \cdot \hat{\boldsymbol{\nu}})_i$. Collecting the results, the expression of the internal power reduces to

$$\begin{aligned} \Pi_{int} = &-\int_\Lambda M^{\rho\beta}{}_{|\rho\beta}\, \dot{w}\, \sqrt{g} \mathrm{d}\Lambda - \sum_i \left[M^{s\nu}\dot{w}_i\right]_0^{L_i} \\ &+\sum_i \left(\int_{\partial\Omega_i} \left(T_i^\nu + \frac{\partial M^{s\nu}}{\partial s} \right) \dot{w}_i\, \mathrm{d}S_i + \int_{\partial\Omega_i} M^{\nu\nu}\dot{\phi}_i\, \mathrm{d}S_i \right). \end{aligned} \tag{21}$$

The external power, with obvious meaning of the symbols, is given by

$$\Pi_{\mathrm{ext}} = \int_\Lambda q\, \dot{w}\, \sqrt{g}\mathrm{d}\Lambda + \sum_j F_j\, \dot{w}_j + \sum_i \left(\int_{\partial\Omega_i} f_i\, \dot{w}_i\, \mathrm{d}S_i + \int_{\partial\Omega_i} m\, \dot{\phi}_i\, \mathrm{d}S_i \right). \tag{22}$$

where the first sum is extended to the corners $\partial\partial\Omega_j$, the second to the sides.

Equating Eqs. (21), (22) one gets the strong form of the equilibrium equations as follows:

$$-M^{\alpha\beta}{}_{|\alpha\beta} = q, \quad on \quad \Omega \tag{23}$$

with boundary conditions on the generic edge $\partial\Omega_i$

$$\begin{aligned} T_i^\nu + \left.\frac{\partial M^{s\nu}}{\partial s}\right|_i &= f_i, \quad or \quad w_i \text{ assigned}, \\ M^{\nu\nu} &= m, \quad or \quad \phi_i \text{ assigned}, \end{aligned} \tag{24}$$

and on the generic corner $\partial\partial\Omega_i$

$$[\![M^{s\nu}]\!]_i = F_i, \quad or \quad w_i \text{ assigned}. \tag{25}$$

being F_i a concentrated force acting at the corner.

The configuration of the boundary of the Kirchhoff plate turns out to be a two-fields manifold, defined by the vertical displacement w_i of the edge curve and by the rotation ϕ_i around the edge, analogously to the kinematics of an Euler-Bernoulli rod as described in [27,28,34,35]. Therefore, the edge rotation ϕ_i must be considered as an independent field for the model. The theoretical motivation of this fact can be found in the more general contest of higher gradient continuum theories, see [36–38] for the details of the generalization of the *Green–Gauss–Ostrogradsky* formula to higher-order theories on manifolds.

Observation: The torsional curvature, given by the mixed component of the covariant derivative (7), is continuous in the plate domain, the derivative of the edge rotation along the side on the two edges merging at the same corner are not equal in general. Indeed evaluating these derivatives along edges 1, 2, that meet at corner 1 (see Fig. 1), we find:

– for the side 2:

$$\begin{aligned}\frac{1}{\|\mathbf{t}_1\|}\frac{\partial\phi(\theta^1,0)}{\partial\theta^1} &= \frac{1}{\|\mathbf{t}_1\|}\frac{\partial}{\partial\theta^1}\left(\frac{\partial w}{\partial\theta^\alpha}\mathbf{t}^\alpha\cdot\hat{\boldsymbol{\nu}}_2\right)\\ &= \frac{1}{\|\mathbf{t}_1\|}\frac{\partial^2 w}{\partial\theta^\alpha\partial\theta^1}\mathbf{t}^\alpha\cdot\hat{\boldsymbol{\nu}}_2 + \frac{1}{\|\mathbf{t}_1\|}\frac{\partial w}{\partial\theta^\alpha}\frac{\partial\mathbf{t}^\alpha}{\partial\theta^1}\cdot\hat{\boldsymbol{\nu}}_2\\ &= \frac{1}{\|\mathbf{t}_1\|}\left(\frac{\partial^2 w}{\partial\theta^\alpha\partial\theta^1} - \frac{\partial w}{\partial\theta^\rho}\Gamma^\rho_{1\alpha}\right)\mathbf{t}^\alpha\cdot\hat{\boldsymbol{\nu}}_2\\ &= \frac{1}{\|\mathbf{t}_1\|}\left(\chi_{11}\mathbf{t}^1\cdot\hat{\boldsymbol{\nu}}_2 + \chi_{12}\mathbf{t}^2\cdot\hat{\boldsymbol{\nu}}_2\right)\\ &= -\left(\chi_{11}\frac{\mathbf{t}^1\cdot\mathbf{t}^2}{\|\mathbf{t}^2\|\|\mathbf{t}_1\|} + \chi_{12}\frac{\|\mathbf{t}^2\|}{\|\mathbf{t}_1\|}\right).\end{aligned} \tag{26}$$

– for the side 1:

$$\begin{aligned}\frac{1}{\|\mathbf{t}_2\|}\frac{\partial\phi(0,\theta^2)}{\partial\theta^2} &= \frac{1}{\|\mathbf{t}_2\|}\frac{\partial}{\partial\theta^2}\left(\frac{\partial w}{\partial\theta^\alpha}\mathbf{t}^\alpha\cdot\hat{\boldsymbol{\nu}}_1\right)\\ &= \frac{1}{\|\mathbf{t}_2\|}\left(\chi_{21}\mathbf{t}^1\cdot\hat{\boldsymbol{\nu}}_1 + \chi_{22}\mathbf{t}^2\cdot\hat{\boldsymbol{\nu}}_1\right)\\ &= -\left(\chi_{21}\frac{\|\mathbf{t}^1\|}{\|\mathbf{t}_2\|} + \chi_{22}\frac{\mathbf{t}^1\cdot\mathbf{t}^2}{\|\mathbf{t}^1\|\|\mathbf{t}_2\|}\right).\end{aligned} \tag{27}$$

Therefore, observing that $\frac{\|\mathbf{t}_1\|}{\|\mathbf{t}^2\|} = \frac{\|\mathbf{t}_2\|}{\|\mathbf{t}^1\|} = \mathbf{t}_1\times\mathbf{t}_2\cdot\hat{\mathbf{n}}$, the derivatives of the normal rotation along the edges are equal at a corner (corner 1 in the example) only if the parametric lines are orthogonal at that corner ($\mathbf{t}^1\cdot\mathbf{t}^2 = 0$).

3 Numerical formulation

In this section, first we give the definition for the G^1-continuity, successively the bi-cubic Coons patch and its rational Gregory's enhancement is presented, see [24,25,39,40]. Finally, the CG^1-formulation for the rational approximant of the displacement of the plate is presented.

3.1 Definition of G^1-continuity

Two space curves $\mathbf{c}_i(\theta)$ are said to meet with parametric continuity (or C^1-continuity), if the parametric tangent vectors, $\mathbf{t}_i = \frac{\mathrm{d}\mathbf{c}_i}{\mathrm{d}\theta}$, are the same at their junction; therefore, under a generic re-parametrization of the curves the parametric continuity is destroyed, thus the parametric continuity is not an intrinsic property. Contrarily, two curves meet with geometric continuity of first degree, G^1-continuity, if the unit tangents are the same at the joint, i.e., if the end rotations are the same [41]. The geometric continuity is an intrinsic property, in the sense that it is invariant under a generic re-parametrization of the curve.

On the basis of the previous observations in [28], we have proposed an implicit G^1-interpolation for a Kirchhoff rod model based on the physical concept of the end rotations, yielding a generalization of the Hermitian interpolation. In this work, we extend the previous idea to the case of surfaces.

Two surfaces with a common boundary curve are called G^1-continuous if *they have a continuously varying tangent plane along that boundary curve*, see [24,40]. This condition represents the continuity requirement to the design of a multi-patch approximant of the displacement of a plate element. Unfortunately, such continuity cannot be achieved with bi-Hermitian interpolation on arbitrarily distorted elements, unless the mesh is C^1-conforming (see [5] who designed a conforming bi-Hermitean plate element under this hypothesis).

Indeed, for an arbitrary quadrilateral mesh, at least 20 degree of freedom are needed for obtaining a G^1-continuous deformation, since on each side has to be guaranteed the continuity of both the position and of the normal derivative.

Historically, the first contribution for generating G^1-continuous multi-patch surfaces was given by S.A. Coons in the context of CAGD, who in 1967 presented a method that uses as input the boundary data sets but that, however, suffers of the same limitation characterizing the bi-Hermitian interpolation, i.e., it fails for meshes not G^1-continuous. In 1974, Gregory presented a generalization of the bi-cubically Coons interpolation that achieves G^1-continuity, consisting in a rational enhancement of the bi-cubic Bezier's interpolation [25]. In [40], considering additional constraint conditions, Farin and Hansford have extended Gregory's patch approach to triangular patches. Next, we describe a procedure for designing a formulation for the plate bending problem that implicitly satisfies G^1-conformity that will be referred to CG^1-formulation. The procedure presented in the paper is limited to G^1-continuous meshes, i.e., meshes obtained by the intersection of two family of lines see [24].

3.2 Bézier's tensor product surface

Indicating by $\theta \in (0,1)$ a parametric coordinate, and with $\mathbf{B}^n(\theta)$ the vector of the nth-order Bernstein polynomials, given by:

$$\boldsymbol{B}^n(\theta) = \{B_j^n(\theta)\}, \quad B_j^n(\theta) = \frac{n!}{j!(n-j)!}(\theta)^j(1-\theta)^{n-j}, \tag{28}$$

with $j = 0, .., n$, a Bézier's curve $\mathbf{c}(\theta)$ is given by the linear combination of the $n+1$ basis functions with $n+1$ control points $\mathbf{P}_j$,

$$\mathbf{c}(\theta) = \sum_{i=0}^{n} B_i^n(\theta)\mathbf{P}_i. \tag{29}$$

The Bézier's representation of a surface is given by the tensor product of two Bézier's curves:

$$\mathbf{p}^{m,n}(\theta^1,\theta^2) = \boldsymbol{B}^m(\theta^1)\,\boldsymbol{P}\,\boldsymbol{B}^{nT}(\theta^2), \tag{30}$$

where $\boldsymbol{P}$ is the matrix of the control points with n-columns and m-rows

$$\boldsymbol{P} = \begin{pmatrix} \mathbf{P}_{00} & \cdots & \mathbf{P}_{0n} \\ \vdots & & \vdots \\ \mathbf{P}_{m0} & \cdots & \mathbf{P}_{mn} \end{pmatrix}. \tag{31}$$

If $n = 3$, we have the bi-cubic Bernstein (or Bézier) basis functions. A transformation of the Bézier's basis leads to the Hermite basis functions:

$$\begin{aligned} &\mathbf{H}(\theta) = \{H_1(\theta), H_2(\theta), H_3(\theta), H_4(\theta)\} \\ &H_1(\theta) = B_0^3(\theta) + B_1^3(\theta) \qquad H_2(\theta) = \frac{B_1^3(\theta)}{3} \\ &H_3(\theta) = -\frac{B_2^3(\theta)}{3} \qquad H_4(\theta) = B_2^3(\theta) + B_3^3(\theta) \end{aligned} \tag{32}$$

that allow to represent a curve $\mathbf{c}(\theta)$ as

$$\mathbf{c}(\theta) = H_1(\theta)\,\mathbf{c}(0) + H_2(\theta)\,\left.\frac{\partial \mathbf{c}}{\partial \theta}\right|_0 + H_3(\theta)\,\left.\frac{\partial \mathbf{c}}{\partial \theta}\right|_1 + H_4(\theta)\,\mathbf{c}(1). \tag{33}$$

3.3 The bi-cubical Coons patch

Coons presented his interpolation (Coons patch) for generic surfaces. We adopt the same description, and successively, we particularize it to the case of plate deformation, characterized only by the normal component of the displacement.

Coons proposed to interpolate a quadrilateral surface between assigned edges, connecting them by means of blending functions. The edge curves can be enhanced with more information, as for instance higher-order derivatives along the edge in order to obtain the required continuity. The Hermite interpolation functions can

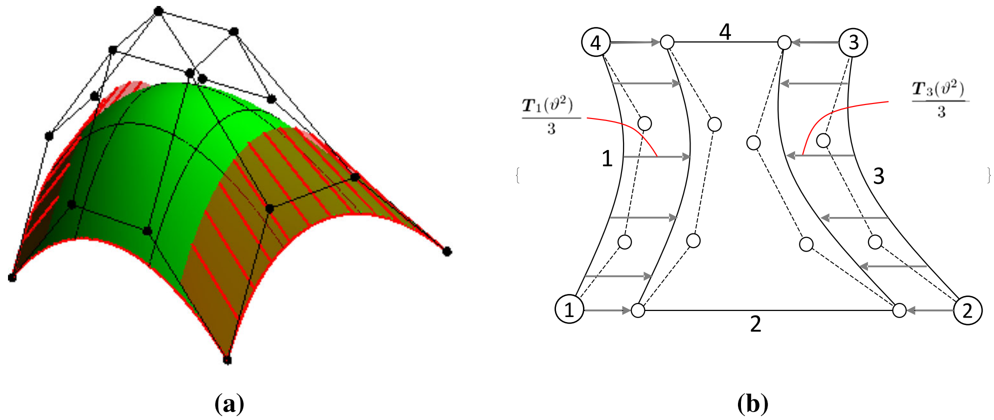

Fig. 2 Ribbons definitions for a bi-cubic Bezier's interpolation: **a** 3D visualization of the ribbons on the deformed configuration, **b** numbering of the sides and ribbon in reference configuration

be used as a natural choice for the blending functions when the normal slope along the edges is required to be continuous.

Coons introduced his interpolation in terms of the boundary ribbons $\mathbf{r}_i$ defined as (see Fig. 2a)

$$\begin{aligned} \mathbf{r}_i = \mathbf{p}_i(\theta^\alpha) + \theta^\beta \mathbf{T}_i(\theta^\alpha) \quad & i = 1, \ldots, 4 \\ & \alpha = 1, \beta = 2 \text{ if } i = 2, 4 \\ & \alpha = 2, \beta = 1 \text{ if } i = 1, 3 \end{aligned} \tag{34}$$

with

$$\begin{aligned} \mathbf{p}_1(\theta^2) &= \mathbf{p}(0, \theta^2), \quad \mathbf{T}_1(\theta^2) = \left.\frac{\partial \mathbf{p}(\theta^1, \theta^2)}{\partial \theta^1}\right|_{\theta^1=0}, \\ \mathbf{p}_2(\theta^1) &= \mathbf{p}(\theta^1, 0), \quad \mathbf{T}_2(\theta^1) = \left.\frac{\partial \mathbf{p}(\theta^1, \theta^2)}{\partial \theta^2}\right|_{\theta^2=0}, \\ \mathbf{p}_3(\theta^2) &= \mathbf{p}(1, \theta^2), \quad \mathbf{T}_3(\theta^2) = \left.\frac{\partial \mathbf{p}(\theta^1, \theta^2)}{\partial \theta^1}\right|_{\theta^1=1}, \\ \mathbf{p}_4(\theta^1) &= \mathbf{p}(\theta^1, 1), \quad \mathbf{T}_4(\theta^1) = \left.\frac{\partial \mathbf{p}(\theta^1, \theta^2)}{\partial \theta^2}\right|_{\theta^2=1}. \end{aligned} \tag{35}$$

From (35), the following identities for the boundary ribbons at the corners are obtained

$$\begin{aligned} \mathbf{T}_1(0) &= \left.\frac{\partial \mathbf{p}_2(\theta^1)}{\partial \theta^1}\right|_0, \quad \mathbf{T}_2(0) = \left.\frac{\partial \mathbf{p}_1(\theta^2)}{\partial \theta^2}\right|_0, \\ \mathbf{T}_2(1) &= \left.\frac{\partial \mathbf{p}_3(\theta^2)}{\partial \theta^2}\right|_0, \quad \mathbf{T}_3(0) = \left.\frac{\partial \mathbf{p}_2(\theta^1)}{\partial \theta^1}\right|_1, \\ \mathbf{T}_3(1) &= \left.\frac{\partial \mathbf{p}_4(\theta^1)}{\partial \theta^1}\right|_1, \quad \mathbf{T}_4(1) = \left.\frac{\partial \mathbf{p}_3(\theta^2)}{\partial \theta^2}\right|_1, \\ \mathbf{T}_4(0) &= \left.\frac{\partial \mathbf{p}_1(\theta^2)}{\partial \theta^2}\right|_1, \quad \mathbf{T}_1(1) = \left.\frac{\partial \mathbf{p}_4(\theta^1)}{\partial \theta^1}\right|_0. \end{aligned} \tag{36}$$

The boundary ribbons of the reference configuration (divided by 3 for clearness) are represented in Fig. 2b. Note that the tangent vectors $\mathbf{T}_i$ join the first two interpolating curves of the plate, not the first two control points. Blending the boundary data sets along the parametric directions two surfaces are obtained, whose expressions, using the definitions (35), are:

$$\begin{aligned} \Pi_{\mathbf{1}}(\mathbf{p})(\theta^1, \theta^2) &= \mathbf{H}(\theta^2)\{\mathbf{p}_2(\theta^1), \mathbf{T}_2(\theta^1), \mathbf{T}_4(\theta^1), \mathbf{p}_4(\theta^1)\}^{\mathrm{T}}, \\ \Pi_{\mathbf{2}}(\mathbf{p})(\theta^1, \theta^2) &= \mathbf{H}(\theta^1)\{\mathbf{p}_1(\theta^2), \mathbf{T}_1(\theta^2), \mathbf{T}_3(\theta^2), \mathbf{p}_3(\theta^2)\}^{\mathrm{T}}. \end{aligned} \tag{37}$$

Summing up the two interpolations (37), it is obtained a surface that does not match the required values at the corners (actually they are doubled), and the inconsistency is removed subtracting a bi-Hermitian interpolation built with the same data set:

$$\Pi_{\mathbf{12}}(\theta^1,\theta^2)=\Pi_{\mathbf{1}}\left(\Pi_{\mathbf{2}}(\mathbf{p})(\theta^1,\theta^2)\right)=\mathbf{H}(\theta^1)\mathbf{M}\mathbf{H}^{\mathrm{T}}(\theta^2) \tag{38}$$

where the matrix $\mathbf{M}$ ruling the tensorial product of the Hermite basis functions, accounting for the identities (36), takes the form:

$$\mathbf{M}=\begin{pmatrix}\mathbf{p}(0,0) & \mathbf{T}_2(0) & \mathbf{T}_4(0) & \mathbf{p}(0,1)\\ \mathbf{T}_1(0) & \tau_{00} & \tau_{01} & \mathbf{T}_1(1)\\ \mathbf{T}_3(0) & \tau_{10} & \tau_{11} & \mathbf{T}_3(1)\\ \mathbf{p}(1,0) & \mathbf{T}_2(1) & \mathbf{T}_4(1) & \mathbf{p}(1,1)\end{pmatrix} \tag{39}$$

and

$$\begin{aligned}\tau_{00}&=\left.\frac{\partial\mathbf{T}_1}{\partial\theta^2}\right|_{\theta^2=0}=\left.\frac{\partial}{\partial\theta^2}\left(\frac{\partial\mathbf{p}}{\partial\theta^1}\right)\right|_{0,0}\quad \tau_{10}=\left.\frac{\partial\mathbf{T}_3}{\partial\theta^2}\right|_{\theta^2=0}=\left.\frac{\partial}{\partial\theta^2}\left(\frac{\partial\mathbf{p}}{\partial\theta^1}\right)\right|_{1,0}\\ \tau_{01}&=\left.\frac{\partial\mathbf{T}_1}{\partial\theta^2}\right|_{\theta^2=1}=\left.\frac{\partial}{\partial\theta^2}\left(\frac{\partial\mathbf{p}}{\partial\theta^1}\right)\right|_{0,1}\quad \tau_{11}=\left.\frac{\partial\mathbf{T}_3}{\partial\theta^2}\right|_{\theta^2=1}=\left.\frac{\partial}{\partial\theta^2}\left(\frac{\partial\mathbf{p}}{\partial\theta^1}\right)\right|_{1,1}\end{aligned} \tag{40}$$

The Coons' interpolation is then given by

$$\mathbf{p}(\theta^1,\theta^2)=\Pi_{\mathbf{1}}(\theta^1,\theta^2)+\Pi_{\mathbf{2}}(\theta^1,\theta^2)-\Pi_{\mathbf{12}}(\theta^1,\theta^2). \tag{41}$$

As highlighted in [24,25], the bi-cubic Coons patch (41) in general does not satisfy the G^1-continuity requirements. In order to get continuity of the position and of the edge rotation, the derivative of the edge rotation along two adjacent side must be independent. In the case of Coons' patch, this is not possible, since both rotations are controlled by the same internal control point, as illustrated in Fig. 2a. In 1974, J. Gregory proposed to modify the definitions of the corner twists (40), blending the twists of the two ribbons meeting at the same corner with rational weight functions:

$$\begin{aligned}\tau_{00}&=\left(\frac{\theta^2}{\theta^1+\theta^2}\right)\left.\frac{\partial\mathbf{T}_2(\theta^1)}{\partial\theta^1}\right|_0+\left(\frac{\theta^1}{\theta^1+\theta^2}\right)\left.\frac{\partial\mathbf{T}_1(\theta^2)}{\partial\theta^2}\right|_0,\\ \tau_{10}&=\left(\frac{\theta^2}{(1-\theta^1)+\theta^2}\right)\left.\frac{\partial\mathbf{T}_2(\theta^1)}{\partial\theta^1}\right|_1+\left(\frac{1-\theta^1}{(1-\theta^1)+\theta^2}\right)\left.\frac{\partial\mathbf{T}_3(\theta^2)}{\partial\theta^2}\right|_0,\\ \tau_{01}&=\left(\frac{1-\theta^2}{\theta^1+(1-\theta^2)}\right)\left.\frac{\partial\mathbf{T}_4(\theta^1)}{\partial\theta^1}\right|_0+\left(\frac{\theta^1}{\theta^1+(1-\theta^2)}\right)\left.\frac{\partial\mathbf{T}_1(\theta^2)}{\partial\theta^2}\right|_1,\\ \tau_{11}&=\left(\frac{1-\theta^2}{(1-\theta^1)+(1-\theta^2)}\right)\left.\frac{\partial\mathbf{T}_4(\theta^1)}{\partial\theta^1}\right|_1+\left(\frac{1-\theta^1}{(1-\theta^1)+(1-\theta^2)}\right)\left.\frac{\partial\mathbf{T}_3(\theta^2)}{\partial\theta^2}\right|_1.\end{aligned} \tag{42}$$

The new definition is equivalent to split the internal control points of the quadrilateral patch and to combine them with two rational functions whose sum is 1, so that when the patch has orthogonal edges, the twists of the ribbons converging at the same corner are equal, and the original Coons' patch interpolation is recovered. In Appendix A is reported a proof of the Gregory's interpolation.

3.4 The bi-cubic Coons-Gregory plate interpolation: CG^1-formulation

Considering a plate lying in the plane (x,y) undergoing bending deformation only, the parametric equation of the deformed middle surface is

$$\mathbf{p}=\mathbf{p}_0(\theta^1,\theta^2)+w(\theta^1,\theta^2)\hat{\mathbf{n}} \tag{43}$$

$\mathbf{p}_0$ is the parametric equation of the (plane) reference configuration, and $\hat{\mathbf{n}}$ is the unit normal to the reference plane of the plate. The boundary ribbons become then, using the same notation as in equation (34):

$$\mathbf{r}_i=\mathbf{p}_i(\theta^\alpha)+\theta^\beta\mathbf{T}_i(\theta^\alpha)=\mathbf{p}_{0i}(\theta^\alpha)+w_i(\theta^\alpha)\hat{\mathbf{n}}+\theta^\beta\frac{\partial\mathbf{p}_{0i}}{\partial\theta^\beta}+\theta^\beta\frac{\partial w_i}{\partial\theta^\beta}\hat{\mathbf{n}}. \tag{44}$$

having indicated with w_i the displacement of the i-th edge of the plate. Using the result (5) of the Kirchhoff constraints, we have

$$\frac{\partial w_i}{\partial \theta^\beta} = \boldsymbol{\phi}_i \times \mathbf{t}_\beta \cdot \hat{\mathbf{n}} = \phi_i^\alpha\, \mathbf{t}_\alpha \times \mathbf{t}_\beta \cdot \hat{\mathbf{n}} \tag{45}$$

where $\phi^\alpha\, \mathbf{t}_\alpha$ is the rotation of the plate around the edge, obtained decomposing the rotation vector along the parametric directions,

$$\boldsymbol{\phi} = \phi^1\, \mathbf{t}_1 + \phi^2\, \mathbf{t}_2 = (\boldsymbol{\phi} \cdot \mathbf{t}^1)\, \mathbf{t}_1 + (\boldsymbol{\phi} \cdot \mathbf{t}^2)\, \mathbf{t}_2 \tag{46}$$

Through the latter decomposition, the components of the rotation vector can be related directly to the space framework. Using Eqs. (44) and (45), the boundary ribbons take the form:

$$\begin{gathered} \mathbf{r}_i = \mathbf{p}_{0i}(\theta^\alpha) + \theta^\beta \frac{\partial \mathbf{p}_{0i}}{\partial \theta^\beta} + w_i(\theta^\alpha)\hat{\mathbf{n}} + \theta^\beta \phi^\alpha(\theta^\alpha)(\mathbf{t}_\alpha \times \mathbf{t}_\beta \cdot \hat{\mathbf{n}})\, \hat{\mathbf{n}} \\ \alpha = 2,\ \beta = 1 \quad \text{if} \quad i = 1, 3 \\ \alpha = 1,\ \beta = 2 \quad \text{if} \quad i = 2, 4. \end{gathered} \tag{47}$$

As stated before, in this paper, we formulate a G¹-continuous approximation on a G¹-conforming geometry of the plate, that is, it is assumed that the parametrization $\mathbf{p}_0$ has continuous tangents along the boundaries of the elements.

From equation (47), it appears that the continuity among adjacent elements is guaranteed if the displacement and rotation are the same along the common boundary. The G¹-formulation is then obtained applying the Coons-Gregory scheme to the vertical displacement. Setting for convenience:

$$\mathcal{A}(\theta^1, \theta^2) = \mathbf{t}_1 \times \mathbf{t}_2 \cdot \hat{\mathbf{n}} \tag{48}$$

(that represents the Jacobian, the area of the element formed by the covariant basis vectors) we have:

$$\begin{aligned} w_1 &= H_1(\theta^2) w_{00} + H_2(\theta^2)\phi^1_{00}\mathcal{A}(0,0) + H_3(\theta^2)\phi^1_{01}\mathcal{A}(0,1) + H_4(\theta^2) w_{01} \\ w_2 &= H_1(\theta^1) w_{00} + H_2(\theta^1)\phi^2_{00}(-\mathcal{A}(0,0)) + H_3(\theta^1)\phi^2_{10}(-\mathcal{A}(1,0)) + H_4(\theta^1) w_{10} \\ w_3 &= H_1(\theta^2) w_{10} + H_2(\theta^2)\phi^1_{10}\mathcal{A}(1,0) + H_3(\theta^2)\phi^1_{11}\mathcal{A}(1,1) + H_4(\theta^2) w_{11} \\ w_4 &= H_1(\theta^1) w_{01} + H_2(\theta^1)\phi^2_{01}(-\mathcal{A}(0,1)) + H_3(\theta^1)\phi^2_{11}(-\mathcal{A}(1,1)) + H_4(\theta^1) w_{11} \end{aligned} \tag{49}$$

and

$$\begin{aligned} \frac{\partial w_1}{\partial \theta^1} &= H_1(\theta^2)\, \phi^2_{00}\, (-\mathcal{A}(0,\theta^2)) + H_2(\theta^2)\, \frac{\partial \phi^2}{\partial \theta^2}\bigg|_{00} (-\mathcal{A}(0,\theta^2)) \\ &\quad + H_3(\theta^2)\, \frac{\partial \phi^2}{\partial \theta^2}\bigg|_{01} (-\mathcal{A}(0,\theta^2)) + H_4(\theta^2)\, \phi^2_{01}\, (-\mathcal{A}(0,\theta^2)), \\ \frac{\partial w_2}{\partial \theta^2} &= H_1(\theta^1)\, \phi^1_{00}\, \mathcal{A}(\theta^1,0) + H_2(\theta^1)\, \frac{\partial \phi^1}{\partial \theta^1}\bigg|_{00} \mathcal{A}(\theta^1,0) \\ &\quad + H_3(\theta^1)\, \frac{\partial \phi^1}{\partial \theta^1}\bigg|_{10} \mathcal{A}(\theta^1,0) + H_4(\theta^1)\, \phi^1_{10}\, \mathcal{A}(\theta^1,0), \\ \frac{\partial w_3}{\partial \theta^1} &= H_1(\theta^2)\, \phi^2_{10}\, (-\mathcal{A}(1,\theta^2)) + H_2(\theta^2)\, \frac{\partial \phi^2}{\partial \theta^2}\bigg|_{10} (-\mathcal{A}(1,\theta^2)) \\ &\quad + H_3(\theta^2)\, \frac{\partial \phi^2}{\partial \theta^2}\bigg|_{11} (-\mathcal{A}(1,\theta^2)) + H_4(\theta^2)\, \phi^2_{11}\, (-\mathcal{A}(1,\theta^2)), \\ \frac{\partial w_4}{\partial \theta^2} &= H_1(\theta^1)\, \phi^1_{01}\, \mathcal{A}(\theta^1,1) + H_2(\theta^1)\, \frac{\partial \phi^1}{\partial \theta^1}\bigg|_{01} \mathcal{A}(\theta^1,1) \\ &\quad + H_3(\theta^1)\, \frac{\partial \phi^1}{\partial \theta^1}\bigg|_{11} \mathcal{A}(\theta^1,1) + H_4(\theta^1)\, \phi^1_{11}\, \mathcal{A}(\theta^1,1). \end{aligned} \tag{50}$$

The G^1-approximation is then given by:

$$w(\theta^1, \theta^2) = \Pi_{\mathbf{1}}(w) + \Pi_{\mathbf{2}}(w) - \Pi_{\mathbf{12}}(w), \tag{51}$$

in which:

$$\begin{aligned}
\Pi_{\mathbf{1}}(w) &= \mathbf{H}(\theta^2)\left\{w_2(\theta^1), \frac{\partial w_2}{\partial \theta^2}, \frac{\partial w_4}{\partial \theta^2}, w_4(\theta^1)\right\}^{\mathrm{T}}, \\
\Pi_{\mathbf{2}}(w) &= \mathbf{H}(\theta^1)\left\{w_1(\theta^2), \frac{\partial w_1}{\partial \theta^1}, \frac{\partial w_3}{\partial \theta^1}, w_3(\theta^2)\right\}^{\mathrm{T}}, \\
\Pi_{\mathbf{12}}(w) &= \mathbf{H}(\theta^1)\mathbf{M}_w\mathbf{H}^{\mathrm{T}}(\theta^2).
\end{aligned} \tag{52}$$

The matrix $\mathbf{M}_w$, using (45) for evaluating the derivatives of the displacement as function of the rotations, is

$$\mathbf{M}_w = \begin{pmatrix} w_{00} & \phi^1_{00}\mathcal{A}(0,0) & \phi^1_{01}\mathcal{A}(0,1) & w_{01} \\ -\phi^2_{00}\mathcal{A}(0,0) & \tau_{00} & \tau_{01} & -\phi^2_{01}\mathcal{A}(0,1) \\ -\phi^2_{01}\mathcal{A}(0,1) & \tau_{10} & \tau_{11} & -\phi^2_{11}\mathcal{A}(1,1) \\ w_{10} & \phi^1_{01}\mathcal{A}(0,1) & \phi^1_{11}\mathcal{A}(1,1) & w_{11} \end{pmatrix} \tag{53}$$

The corner twists are evaluated according to Gregory's enhancement (42) as:

$$\begin{aligned}
\tau_{00} &= \left(\frac{\theta^1}{\theta^1+\theta^2}\right)\frac{\partial \phi^2}{\partial \theta^2}\bigg|_{00}(-\mathcal{A}(0,0)) + \left(\frac{\theta^2}{\theta^1+\theta^2}\right)\frac{\partial \phi^1}{\partial \theta^1}\bigg|_{00}\mathcal{A}(0,0), \\
\tau_{10} &= \left(\frac{1-\theta^1}{(1-\theta^1)+\theta^2}\right)\frac{\partial \phi^2}{\partial \theta^2}\bigg|_{10}(-\mathcal{A}(1,0)) + \left(\frac{\theta^2}{(1-\theta^1)+\theta^2}\right)\frac{\partial \phi^1}{\partial \theta^1}\bigg|_{10}\mathcal{A}(1,0), \\
\tau_{01} &= \left(\frac{\theta^1}{\theta^1+(1-\theta^2)}\right)\frac{\partial \phi^2}{\partial \theta^2}\bigg|_{01}(-\mathcal{A}(0,1)) + \left(\frac{1-\theta^2}{\theta^1+(1-\theta^2)}\right)\frac{\partial \phi^1}{\partial \theta^1}\bigg|_{01}\mathcal{A}(0,1), \\
\tau_{11} &= \left(\frac{1-\theta^1}{(1-\theta^1)+(1-\theta^2)}\right)\frac{\partial \phi^2}{\partial \theta^2}\bigg|_{11}(-\mathcal{A}(1,1)) + \left(\frac{1-\theta^2}{(1-\theta^1)+(1-\theta^2)}\right)\frac{\partial \phi^1}{\partial \theta^1}\bigg|_{11}\mathcal{A}(1,1).
\end{aligned} \tag{54}$$

The element so obtained has 20 degrees of freedom, five for each corner, the corner's displacements, the two components of the rotation and the two parametric side derivatives of the two edge rotations:

$$\begin{aligned}
\mathbf{q}_1 &= \left\{w_{00}, \phi^x_{00}, \phi^y_{00}, \frac{\partial \phi^1}{\partial \theta^1}\bigg|_{0,0}, \frac{\partial \phi^2}{\partial \theta^2}\bigg|_{0,0}\right\}, \\
\mathbf{q}_2 &= \left\{w_{10}, \phi^x_{10}, \phi^y_{10}, \frac{\partial \phi^1}{\partial \theta^1}\bigg|_{1,0}, \frac{\partial \phi^2}{\partial \theta^2}\bigg|_{1,0}\right\}, \\
\mathbf{q}_3 &= \left\{w_{11}, \phi^x_{11}, \phi^y_{11}, \frac{\partial \phi^1}{\partial \theta^1}\bigg|_{1,1}, \frac{\partial \phi^2}{\partial \theta^2}\bigg|_{1,1}\right\}, \\
\mathbf{q}_4 &= \left\{w_{01}, \phi^x_{01}, \phi^y_{01}, \frac{\partial \phi^1}{\partial \theta^1}\bigg|_{0,1}, \frac{\partial \phi^2}{\partial \theta^2}\bigg|_{0,1}\right\},
\end{aligned} \tag{55}$$

and finally: $\mathbf{q} = \{\mathbf{q}_1, \mathbf{q}_2, \mathbf{q}_3, \mathbf{q}_4\}$. The rational functions are continuous at the corners and have continuous first derivatives, but the second derivatives are discontinuous at the corner to which the function is related. On the basis of the Bézier's projection, see [42,43], the CG^1-formulation can be generalized to the B-spline representation. The proposed formulation can be useful to design finite element for modeling smoothed localization as occurs in high gradient damage model, see [44].

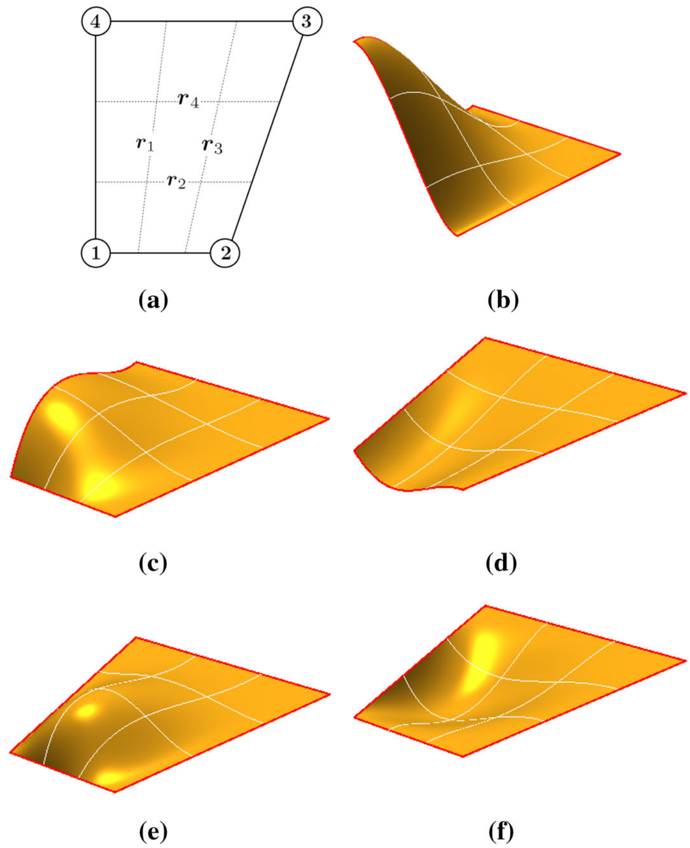

Fig. 3 Initial geometry and G^1-shape-functions of the Coons-Gregory's interpolation for the five degrees of freedom relative to the first corner node. (MF = Magnification Factor). **a** Initial geometry. **b** $w_1 = 1$, (MF = 1). **c** $\phi_{1,x} = 1$, (MF = 5). **d** $\phi_{1,y} = 1$, (MF = 5). **e** $\partial_{\theta^2}\phi^1 = 1$, (MF = 50). **f** $\partial_{\theta^1}\phi^2 = 1$, (MF = 50)

3.5 An example of a Coons' interpolation for a plate

In order to clarify the interpolation presented in the previous section, we consider the plate represented in Fig. 3a; the coordinates of the corners are $\boldsymbol{p}_{0_1} = \{0, 0\}$, $\boldsymbol{p}_{0_2} = \{0.25, 0\}$, $\boldsymbol{p}_{0_3} = \{0.5, 0.5\}$ and $\boldsymbol{p}_{0_4} = \{0, 0.5\}$. In Fig. 3 are represented the first five shape functions, associated with the degrees of freedom of the first corner.

4 Numerical investigations

In this section, some plate problems modeled by CG^1-formulation based on the Coons-Gregory rational approximant space are analyzed. The examples will be used to verify the fulfillment of G^1-continuity particularly on distorted geometries using structured meshes. In addition, the accuracy and the rate of convergence of the solution will be presented, and compared with efficient finite elements available in the literature. The performance of the element will be evaluated calculating the rate of convergence of the energy error. It is recalled that for a complete interpolation of degree k with a variational index of the problem equal to 2, the theoretic rate of convergence of the energy norm is $k - 1$ if no singularities are present. In the plots for convenience is reported the relative error on the strain energy and not its norm; therefore, the ideal rate of convergence expected is $2(k - 1)$. Gauss quadrature was used for evaluating the integrals, adopting $p + 1 = 4$ Gauss points in each direction.

4.1 Square-plate

First, we consider a square plate with a non uniform structured mesh characterized by the mesh distortion parameter a, as shown in Fig. 4. The length of the edge of the plate is $L = 1\,[m]$, Young's modulus $E =$

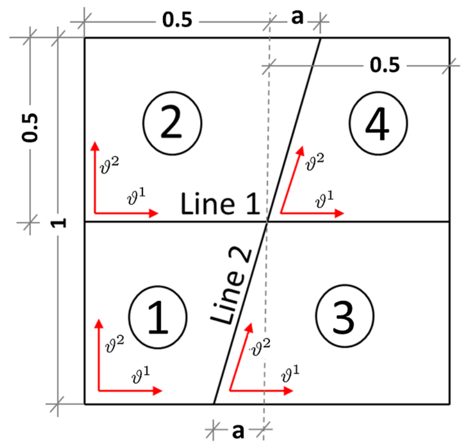

Fig. 4 Geometry and labels of the square plate problem

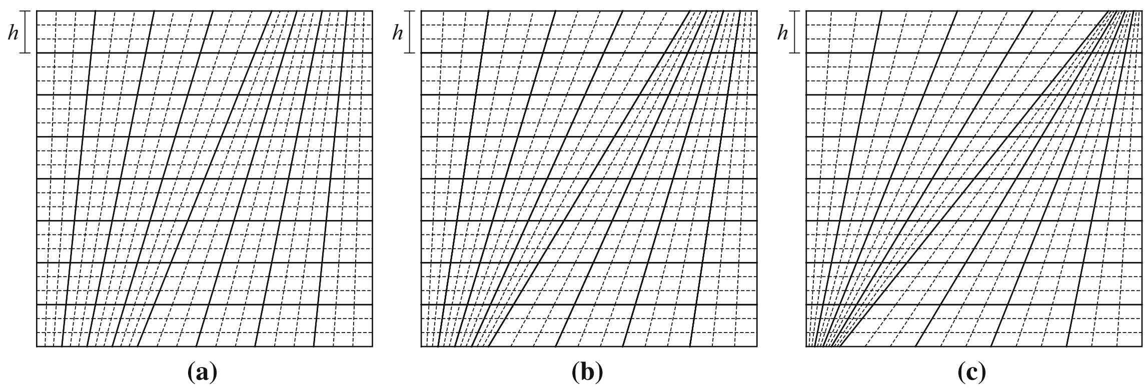

Fig. 5 Square plate: considered distorted un-structured meshes. **a** $a = 0.2$. **b** $a = 0.3$. **c** $a = 0.4$

10^8 $[kN/m^2]$ $\nu = 0.25$ and the thickness is 10^{-4} $[m]$; in Fig. 4 are shown the labels attributed to the patches and to the lines between these patches. For each value of the mesh distortion a, we consider several meshes, obtained dividing each patch in an equal number of elements, and in order to test the G^1-continuity several boundary conditions and different load cases are analyzed. In Fig. 5 are represented the meshes for three values of the distortion parameter a, and a discretization of 8×8 elements. Notice the severe distortion that is achieved when $a = 0.3$ or 0.4.

4.1.1 Simply supported square plate with uniform pressure

First is considered the case of a plate with simply supported boundary conditions loaded by an uniform pressure $q = 1[kN/m^2]$. The exact value of the strain energy for the case at hand is 95.766217011 $[kNm]$.

The rate of convergence of the energy error for several values of the distortion parameter a ranging in the interval (0, 0.4) is presented in Fig. 6a. On the abscissa is reported the characteristic value h of the elements, taken equal to the vertical length of the element at the generic level of refinement. It is found that the rate of convergence achieves its optimal value for any value of the distortion, confirming the robustness of the proposed element. Also the accuracy only slightly decreases for increasing distortion. Figure 6b presents the convergence of the strain energy increasing the number of elements per side of the plate. A convergence from below is obtained, as it was expected since the element is displacement based.

The robustness of the element can also be evaluated from the analysis of the condition number of the stiffness matrix, that is reported in Fig. 7a as a function of the number of elements per side of the plate. As it is expected when the elements are not distorted, the condition number remains constant for all the discretizations. For larger values of the distortion parameters, the condition number degrades when the element size becomes smaller. However, it is observed that even for the most distorted mesh considered, the condition number increases by less than one order of magnitude.

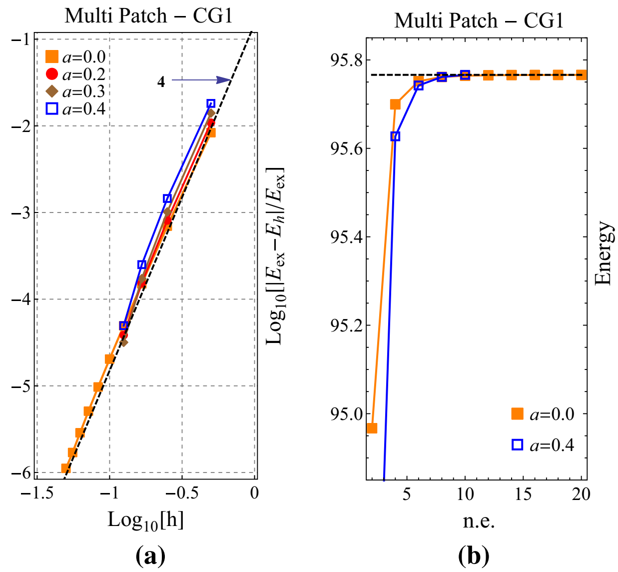

Fig. 6 Simply supported plate with uniform pressure—convergence properties: **a** Rate of convergence for the relative energy error. **b** Convergence for the energy versus the number of the elements per side

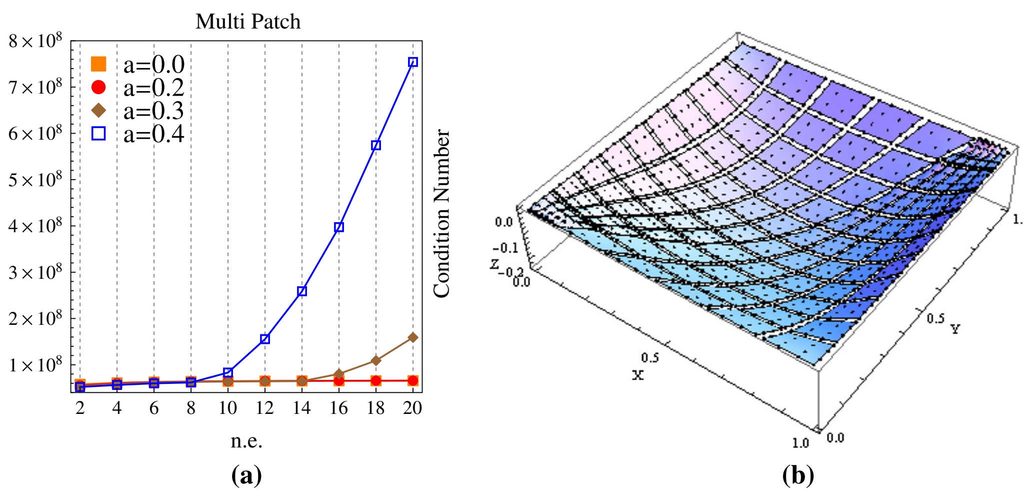

Fig. 7 Simply supported plate with uniform pressure: **a** Condition number of the stiffness matrix. **b** Bending moment M_{xx}

A sketch of the bending moment in the plate, evaluated at the Gauss points, is presented in Fig. 7b.

The deformed configuration for a 4x4 mesh obtained with the conforming CG^1-formulation is shown in Fig. 8a, b, referring to the cases $a = 0, a = 0.4$, from which the continuity of the slope at the element boundaries can be appreciated.

The achievement of the G^1-continuity is further verified with the plots of Fig. 9a, b, where the components of the unit normals to the deformed configuration are plotted along the edge lines 1 and 2, see Fig. 4 using a black and a white line for elements located on either side of the lines. The severe case $a = 0.4$ is considered. The plots perfectly superpose, and the difference in the components of the unit normal vector along the joints is numerically zero.

4.1.2 Clamped square plate with uniform pressure

The second application concerns a clamped plate loaded by a uniform pressure like in the previous case. The exact value of the strain energy for this case is 21.8880043 [kNm]. Figure 10a shows the rate of convergence for different distortions of the mesh. Also, in this case, the optimal rate of convergence is achieved, independently

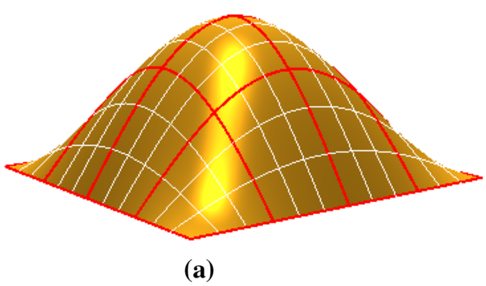

Fig. 8 Simply supported square plate with uniform pressure—magnified deformed configurations obtained with the CG^1-formulation: **a** $a = 0.0$, **b** $a = 0.4$

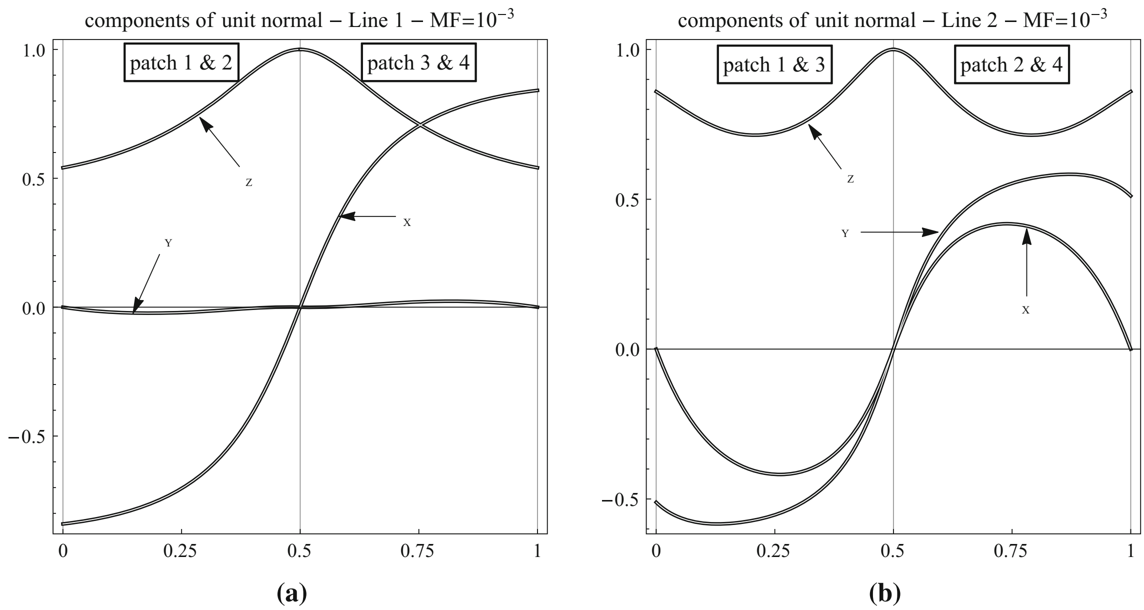

Fig. 9 Simply supported square plate with uniform pressure—components of the unit normal vector along **a** the line 1, **b** the line 2, ($MF = 10^{-3}$)

from the distortion. The loss in the accuracy level for distorted meshes is almost negligible, as can also be observed from the convergence results of Fig. 10b. The deformed configurations of the plate for $a = 0$, $a = 0.4$ are represented in Fig. 10c, d, also in this case the slopes at the boundaries between adjacent elements are perfectly continuous.

4.1.3 Simply supported square plate under central point load

In this subsection, a simply supported square plate is considered subjected to a point force $F = \{0, 0, -1\}$ $[kN]$ at the center. The exact value of the strain energy is $0.652547 * 10^3$ $[kNm]$. A convergence analysis under the h-refinement for the CG^1-formulation is shown in Fig. 11a, in which h represents the element side, for the values $a = 0, 0.2, 0.3, 0.4$. Contrarily to the cases of the plate loaded with an uniform pressure, the rate of convergence obtained is 2. This is due to the fact that in a point loaded plate there is a logarithmic singularity in the solution [45]. However, also in this case, there is no degradation of the rate of convergence introducing distortion in the mesh. The accuracy of the solution, however, is more affected by the distortion with respect to the case of uniform load, as can also been appreciated by the convergence plot of Fig. 11b.

Figure 12a, c present the convergence of the energy error for the cases $a = 0$ and $a = 0.4$, compared with the results obtained by two plate elements of the MITC plate family, MITC4 and MITC9 [22]. These elements

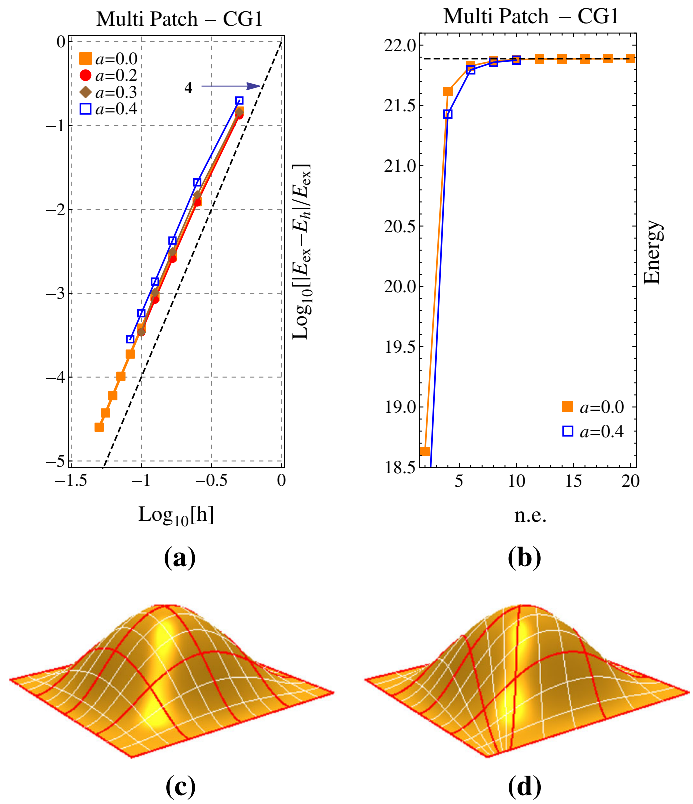

Fig. 10 Clamped plate with uniform pressure—convergence properties: **a** Rate of convergence for the relative energy error, **b** Energy versus the number of elements per side. Magnified deformed configurations: **c** $a = 0.0$, **d** $a = 0.4$

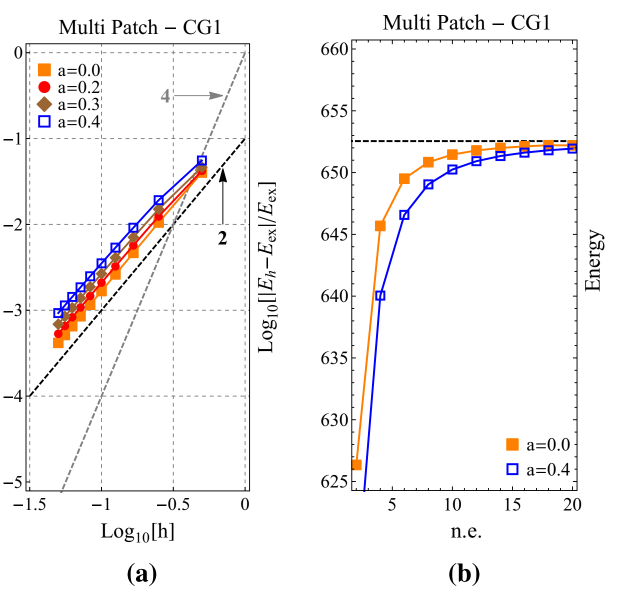

Fig. 11 Simply supported plate with a central point force —convergence properties: **a** Rate convergence for the relative energy error, **b** Convergence for the energy versus the number of elements side

were chosen for the comparison since they are among the best elements available for plates. Since MITC plate are shear deformable, a very small thickness was used in the calculation, in order to make the influence of shear negligible. The rate of convergence of MITC4 is smaller than the one found with the CG^1-formulation, as it

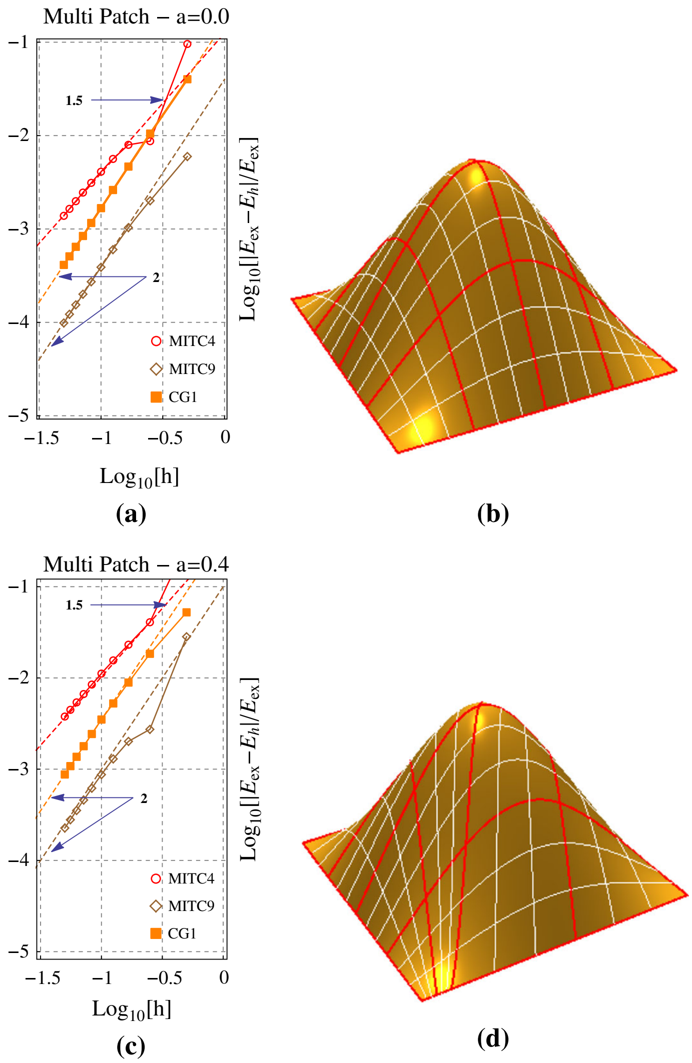

Fig. 12 Simply supported plate with concentrated force—rate of convergence of the energy relative error for the two values of the mesh distortion: **a** $a = 0.0$, **c** $a = 0.4$, and respectively deformed configuration: **b** $a = 0.0$, **d** $a = 0.4$

should be, since MITC4 uses linear interpolations. The rate of convergence of MITC9 is, instead, comparable, showing that the sub-optimal rate of convergence found with the proposed element is due to the singularity present in the solution and not to the formulation. The deformation of the plates for $a = 0,\ 0.4$ are presented in Fig. 12b, d, from which slope continuity can be appreciated.

4.1.4 Clamped square plate with central point load

A vertical force of $1[kN]$ is applied at the center of the clamped plate. The exact strain energy is $3.15676 * 10^2\ [kNm]$. The rate of convergence for $a = 0$, $a = 0.2$, $a = 0.3$, $a = 0.4$ is presented in Fig. 13a. Also in this case, a rate of 2 is obtained, analogously to the case of the simply supported plate, and also similar is the slight degradation of the accuracy that is found for the more distorted meshes.

The convergence for the energy error for $a = 0$, $a = 0.4$ are also in this case compared with the results found with MITC4 and MITC9 elements (Fig. 14a, c). The rate of convergence found with the CG^1-formulation is similar to the one obtained with MITC9, even though the accuracy is somewhat worse.

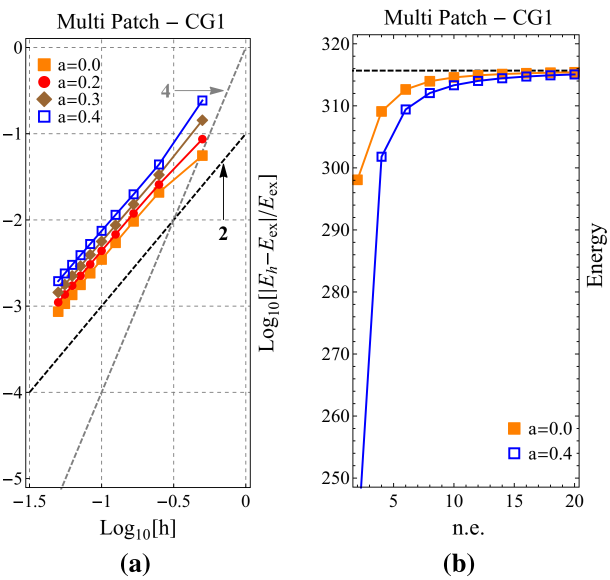

Fig. 13 Clamped plate with a central point force—Convergence properties: **a** Rate of convergence for the relative energy error, **b** Convergence of the energy versus the number of elements per side

4.1.5 Square plate: sensitivity to distortion

In this section, the results obtained in the previous sections are summarized in order to evaluate the influence of the distortion of the structured mesh on the error obtained in the numerical solution. Specifically, the energy error evaluated with a 8×8 mesh is reported against the parameter a in Fig. 15a–d for the cases of the simply supported plate with uniform pressure, clamped plate with uniform pressure, simply supported plate with concentrated load, clamped plate with concentrated load, respectively.

In order to evaluate the results also the energy errors obtained with MITC4 and MITC9 plate elements, which are known to be very robust under mesh distortion, are reported. It can be seen that the proposed element presents a robustness close (in some cases even better) than MITC9, while, at least for plates loaded with uniform pressure, MITC4 shows a grater insensitivity of the error to mesh distortion. Its accuracy, however, is smaller, due to the lower degree of the interpolation. From these comparisons appears the robustness of the proposed CG^1-formulation.

4.2 Patch test: a case with constant bending moments

In this section we consider a square plate with only two simply supported edges and subjected to a unit point force at the free corner. A structured mesh defined by means of the distortion parameter a is considered analogously to the previous case. The relevant data are $L = 1\,[m]$, $E = 10^8\,[kN/m^2]$, $\nu = 0.25$ and a thickness of $10^{-3}\,[m]$. For this set-up, the bending moments M_{xx} and M_{yy} are constantly equal to zero while the twisting moment is constant and equal to $0.5\,[kN/m]$. The convergence analysis for the relative energy error is plotted in Fig. 16a for several values of the distortion parameter.

Although the element does not present severe locking and the solution converges to the exact one, the optimal rate of convergence is not achieved. An enhanced formulation able to pass the patch test will be in subsequent work. The deformed configuration obtained with the CG^1-formulation is depicted in Fig. 16b for a 4×4 mesh.

4.3 Clamped circular plate

In order to show the suitability of the method to treat curved meshes, we consider the case of a circular plate. Two cases of a clamped circular plate are considered, one subjected to an uniform pressure $p = 1\,[kN/m^2]$, the other one subjected to a point force at the center of the plate $F = 1\,[kN]$. The plate has $r = 1\,[m]$,

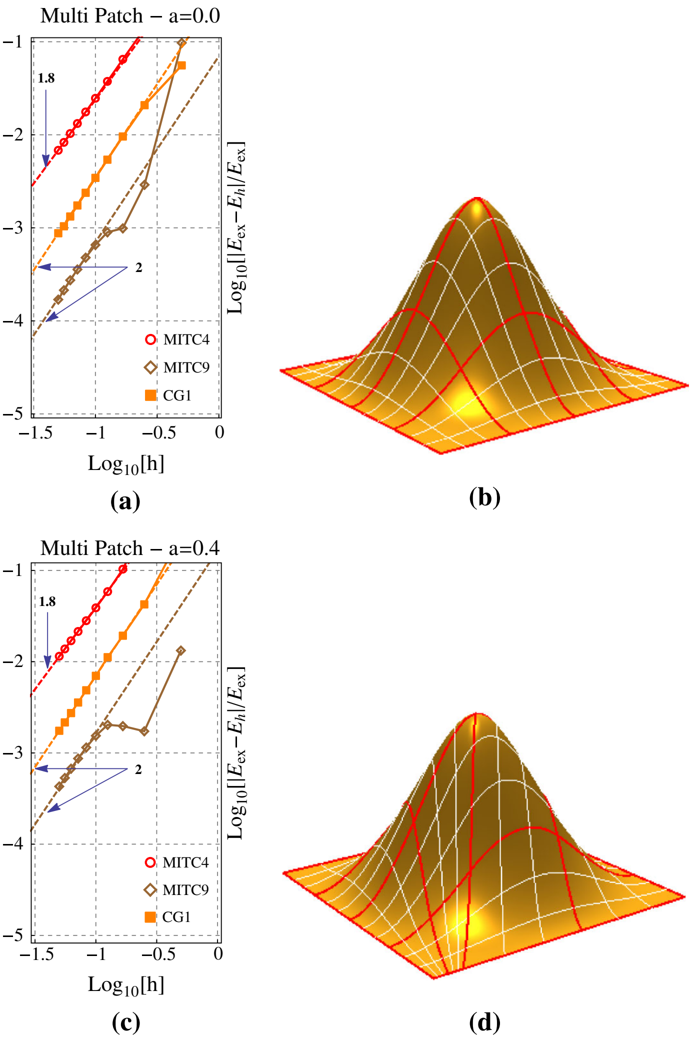

Fig. 14 Clamped square plate with concentrate force—Rate of convergence of the energy relative error for the two values of the mesh distortion: **a** $a = 0.0$, **c** $a = 0.4$, and respectively deformed configuration: **b** $a = 0.0$, **d** $a = 0.4$

$E = 10^8\ [kN/m^2]$, $\nu = 0.25$, and the thickness is $t = 10^{-4}\ [m]$. The structured mesh for this geometry is obtained by an ad hoc deformation of a square geometry.

Continuity of the slopes is again satisfied, as shown in Fig. 17c. The convergence of the energy for the two cases is illustrated in Fig. 17a, b, highlighting the good accuracy obtained in both cases, especially with the uniform pressure.

5 Conclusions and future developments

In this work, starting from a re-visitation of the Gregory's enhancement of the Coons patch interpolation, as in [24,25,39] we have formulated a quadrilateral finite element for the Kirchhoff plate problem that implicitly achieves G^1-continuity strongly, provided that a G^1-conforming structured mesh is considered for the plate geometry description. This has been obtained adopting a rational enhancement of the Hermite interpolation that however presents discontinuities for the curvatures at the four corners.

Analogously to the G^1-strategy presented in [28], in this work the boundary edge rotations are introduced as degrees of freedom in the formulation of the conforming element. In this work, only the bi-cubic interpolation case has been investigated. The obtained element shows the theoretical optimal rate of convergence for the energy error, and appears to be robust and highly accurate also for very distorted structured meshes.

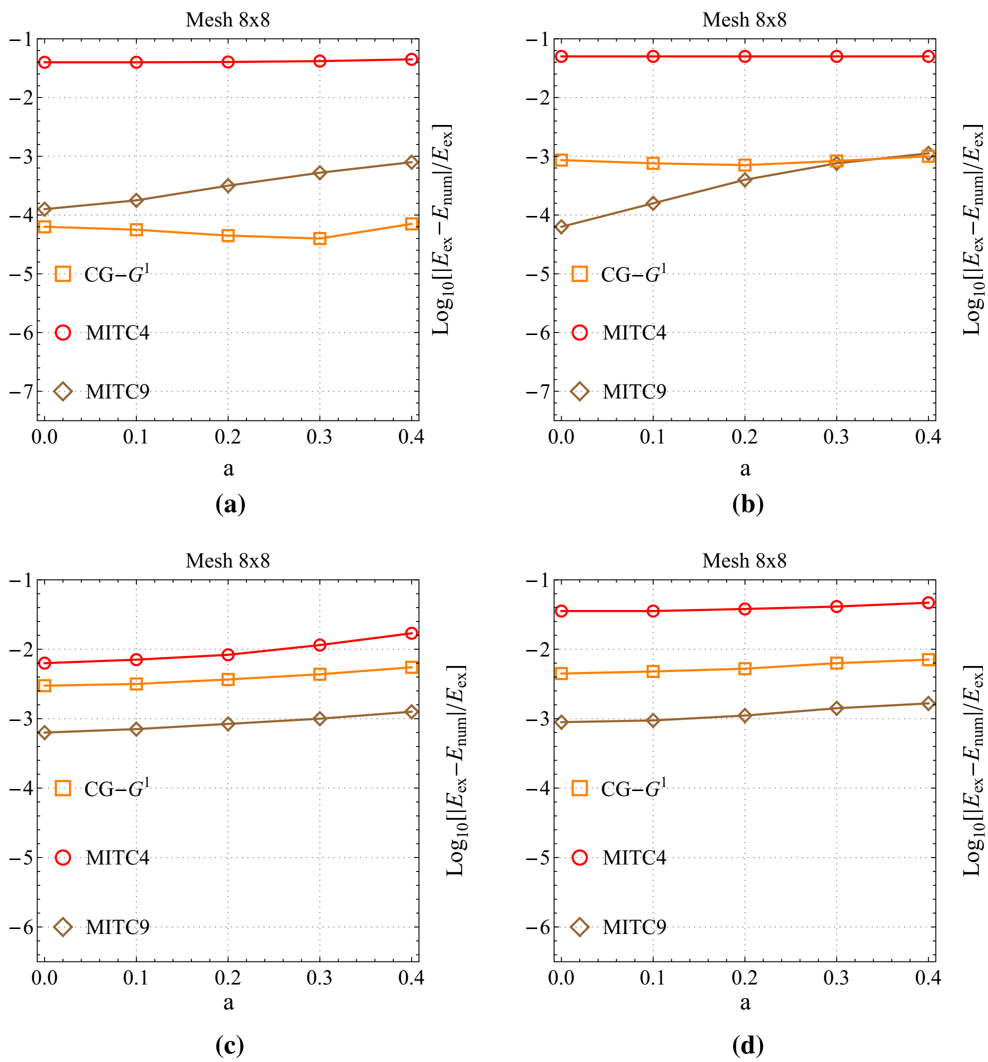

Fig. 15 Sensitivity of the element to the structured mesh distortions. **a** Simply supported plate under uniform pressure. **b** Clamped plate under uniform pressure. **c** Simply supported plate under a central point force. **d** Clamped plate under a central point force

The lack of continuity of the bending curvatures at the corners has been shown to reduce somewhat the rate of convergence for those problems where a constant deformation field is present, i.e., the rational CG^1-formulation does not pass the bending patch test.

Future developments are concerned with the following items:

– Generalization of the proposed CG^1-formulation to general C^0-conforming un-structured meshes.
– Adapt the CG^1-formulation in order to pass the bending patch test.
– Application of the CG^1-formulation to more general Isogeometric formulations.
– Generalization of the CG^1-formulation for the computation of the non-polar shell models.

The CG^1-formulation can be able to design conforming finite elements for the computation in higher gradient elasticity, analogously to [46,47]. Furthermore, the CG^1-formulation naturally take into account edge beam elements and the presence of second gradient terms, it is particularly suitable for computing two-dimensional sheet with embedded fibers as introduced and discussed in [48–52].

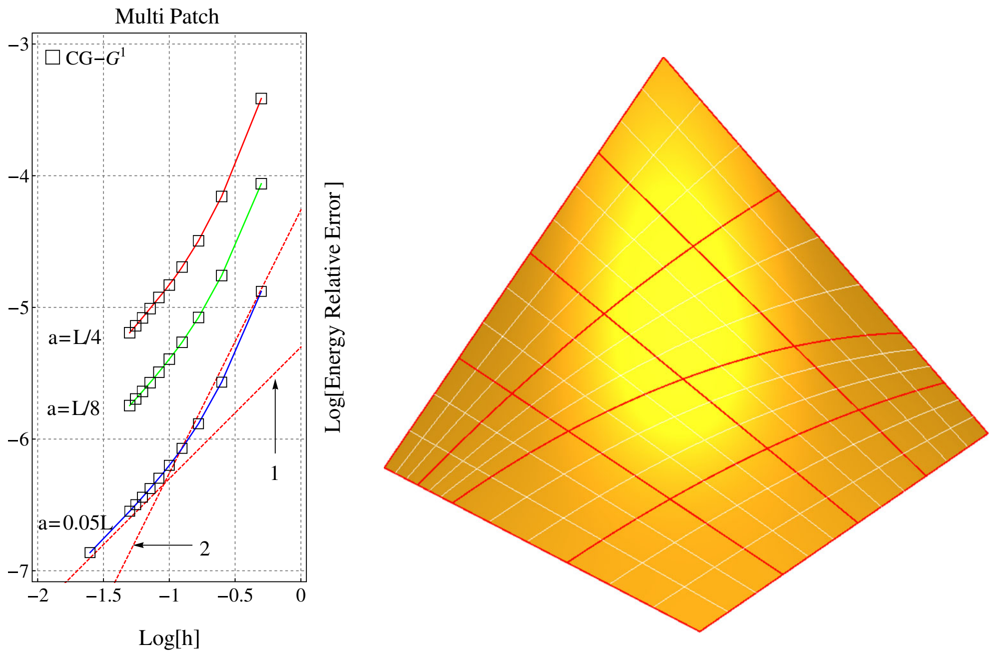

(a) (b)

Fig. 16 Patch test: **a** Convergence analysis of the relative energy error for several a. **b** Deformed configuration obtained for $a = L/4$ with a 4 x 4 structured mesh

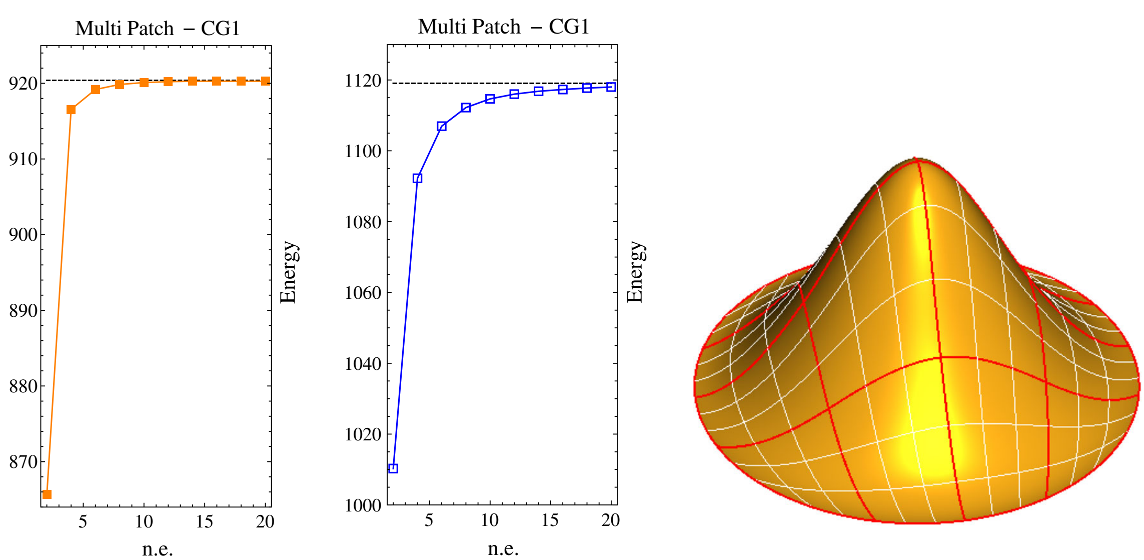

(a) (b) (c)

Fig. 17 Clamped circular plate: **a** Convergence of the energy versus the number of element per side (uniform pressure), **b** Convergence of the energy versus the number of element per side (concentrated force), **c** Deformed configuration (concentrated force)

A Proof of Gregory's interpolation

The proof of Gregory's interpolation can be given by direct check. Referring to edge 1, let's evaluate the derivative of the surface along the line $\theta^1 = 0$ using Coons' interpolation (41):

$$
\begin{aligned}
\left.\frac{\partial \mathbf{p}}{\partial \theta^1}\right|_{\theta^1=0} &= \left.\frac{\partial}{\partial \theta^1}\right|_{\theta^1=0} \left(\Pi_{\mathbf{1}}(w) + \Pi_{\mathbf{2}}(w) - \Pi_{\mathbf{12}}(w)\right) \\
&= \mathbf{T}_1(\theta^2) + H_1(\theta^2)\left.\frac{\partial \mathbf{p}_2}{\partial \theta^1}\right|_0 - H_1(\theta^2)\,\mathbf{T}_1(0) \\
&\quad + H_2(\theta^2)\left.\frac{\partial \mathbf{T}_2}{\partial \theta^1}\right|_0 - H_2(\theta^2)\,\tau_{00} \\
&\quad + H_3(\theta^2)\left.\frac{\partial \mathbf{T}_4}{\partial \theta^1}\right|_0 - H_3(\theta^2)\,\tau_{01} \\
&\quad + H_4(\theta^2)\left.\frac{\partial \mathbf{p}_4}{\partial \theta^1}\right|_0 - H_4(\theta^2)\,\mathbf{T}_1(1).
\end{aligned}
\tag{56}
$$

Accounting for the identities (36) and substituting for the corner twists the expressions (42) all the addends in (56) except the first cancel out. Specifically for the terms involving the twists one has:

$$
\begin{aligned}
& H_2(\theta^2)\left(\left.\frac{\partial \mathbf{T}_2}{\partial \theta^1}\right|_0 - \frac{\theta^1}{\theta^1+\theta^2}\left.\frac{\partial \mathbf{T}_1}{\partial \theta^2}\right|_0 - \frac{\theta^2}{\theta^1+\theta^2}\left.\frac{\partial \mathbf{T}_2}{\partial \theta^1}\right|_0\right)_{\theta^1=0} \\
&\quad = H_2(\theta^2)\left(\frac{\theta^1}{\theta^1+\theta^2}\left.\frac{\partial \mathbf{T}_2}{\partial \theta^1}\right|_0 - \frac{\theta^1}{\theta^1+\theta^2}\left.\frac{\partial \mathbf{T}_1}{\partial \theta^2}\right|_0\right)_{\theta^1=0} = 0, \\
& H_3(\theta^2)\left(\left.\frac{\partial \mathbf{T}_4}{\partial \theta^1}\right|_0 - \frac{\theta^1}{\theta^1+1-\theta^2}\left.\frac{\partial \mathbf{T}_1}{\partial \theta^2}\right|_1 - \frac{1-\theta^2}{\theta^1+1-\theta^2}\left.\frac{\partial \mathbf{T}_4}{\partial \theta^2}\right|_0\right)_{\theta^1=0} \\
&\quad = H_3(\theta^2)\left(\frac{\theta^1}{\theta^1+1-\theta^2}\left.\frac{\partial \mathbf{T}_4}{\partial \theta^1}\right|_0 - \frac{\theta^1}{\theta^1+1-\theta^2}\left.\frac{\partial \mathbf{T}_1}{\partial \theta^2}\right|_1\right)_{\theta^1=0} = 0.
\end{aligned}
\tag{57}
$$

Note that the definitions (42) introduce a discontinuity on the corner torsion, that is

$$
\lim_{\theta^1\to 0}(\tau_{00}) = \left.\frac{\partial \mathbf{T}_1}{\partial \theta^2}\right|_0, \quad \text{and} \quad \lim_{\theta^2\to 0}(\tau_{00}) = \left.\frac{\partial \mathbf{T}_2}{\partial \theta^1}\right|_0.
\tag{58}
$$

References

1. Cottrell, J.A., Hughes, T.J.R., Bazilevs, Y.: Isogeometric Analysis: Toward Integration of CAD and FEA. Wiley, London (2009)
2. Zienkiewicz, O.C., Taylor, R.L.: The Finite Element Method, Fifth Edition, Vol 2: Solid Mechanics, 5th edn. Butterworth-Heinemann, London (2002)
3. Bogner, F.K., Fox, R.L., Schmit, L.A.: The generation of interelement-compatible stiffness and mass matrices by the use of interpolation fomulae. In: Przemienicki, J.S., Bader, R.M., Bozich, W.F., Johnson, J.R., Mykytow, W.J. (eds.) Proceeding of 1st Conference of Matrix Methods in Structural Mechanics. volume AFFDITR-66-80, pp. 397–433. Air Force Flight Dynamics Laboratory, Wright Patterson Air Force Base, OH (1966)
4. de Veubeke, B.F.: A conforming finite element for plate bending. Int. J. Solids Struct. **4**, 95–108 (1968)
5. Petera, J., Pittman, J.F.T.: Isoparametric Hermite elements. Int. J. Numer. Method Eng. **37**, 3489–3519 (1994)
6. Argyris, J.H., Fried, I., Scharpf, D.W.: The TUBA family of plate elements for the matrix displacement method. Aeronaut. J. R. Aeronaut. Soc. **72**, 701–709 (1968)
7. Andreaus, U., dell'Isola, F., Giorgio, I., Placidi, L., Lekszycki, T., Rizzi, N.L.: Numerical simulations of classical problems in two-dimensional (non) linear second gradient elasticity. Int. J. Eng. Sci. **108**, 34–50 (2016)
8. Fischer, P., Mergheim, J., Steinmann, P.: On the C1 continuous discretization of non-linear gradient elasticity: a comparison of NEM and FEM based on Bernstein–Bézier patches. Int. J. Numer. Methods Eng. **82**, 1282–1307 (2010)
9. Wempner, G.A., Oden, J.T., Cross, D.K.: Finite element analysis of thin shells. Proc. ASCE **94**, 1273–1294 (1968)
10. Batoz, J.L., Dhatt, G.: Development of two simple shell elements. AIAA J. **10**(2), 237–238 (1972)
11. Batoz, J.L., Bathe, K.-J., Ho, L.-W.: A study of three-node triangular plate bending elements. Int. J. Numer. Methods Eng. **15**(12), 1771–1812 (1980)
12. Guo, Y.Q., Gati, W., Naceur, H., Batoz, J.L.: An efficient DKT rotation free shell element for springback simulation in sheet metal forming. Comput. Struct. **80**, 2299–2312 (2002)
13. Irons, B.M.: The semi-Loof shell element. In: Ashwell, D.G., Gallagher, R.H. (eds.) Finite Elements for Thin Shells and Curved Members, pp. 197–222. Wiley, Chichester (1976)

14. Clough, R.W., Tocher, J.L.: Finite element stiffness matrices for analysis of plates in bending. In: Przemienicki, J.S., Bader, R.M., Bozich, W.F., Johnson, J.R., Mykytow, W.J. (eds.) Proceedings of Conference on Matrix Methods in Structural Mechanics, volume AFFDL-TR-68-150, pp. 515–545, Air Force Flight Dynamics Laboratory, Wright Patterson Air Force Base, OH (1965)
15. Fraejis de Veubeke, B.: An equilibrium model for plate bending. Int. J. Solids Struct. **4**, 447–468 (1967)
16. Herrmann, L.R.: Finite element bending analysis of plates. In: Proceedings of ASCE, EM-5:13–25 (1968)
17. Pian, T.H.H., Sze, K.Y.: Hybrid stress finite element methods for plate and shell structures. Adv. Struct. Eng. **4**, 13–18 (2001)
18. Zienkiewicz, O.C., Xu, Z., Zeng, L.F., Samuelsson, A., Wiberg, N.-E.: Linked interpolation for reissner-mindlin plate elements: Part I: A simple quadrilateral. Int. J. Numer. Methods Eng. **36**, 3043–3056 (1993)
19. Garusi, E., Tralli, A., Cazzani, A.: An unsymmetric stress formulation for reissner-mindlin plates: a simple and locking-free rectangular element. Int. J. Comput. Eng. Sci. **5**(3), 589–618 (2004)
20. Bathe, K.-J., Dvorkin, E.N.: A formulation ofa general shell elements—the use of mixed interpolation of tensorial components. Int. J. Numer. Methods Eng. **22**, 697–722 (1986)
21. Bathe, K.-J., Brezzi, F.: A simplified analysis of two plate bending elements—the MITC4 and MITC9 elements. In: Pande, G.N., Middleton, J. (eds.) Numerical Techniques for Engineering Analysis and Design, pp. 407–417. Martinus Nijhoff, Amsterdam (1987)
22. Bathe, K.-J., Brezzi, F., Cho, S.W.: The MITC7 and MITC9 plate bending elements. Comput. Struct. **32**(3/4), 797–814 (1989)
23. Bathe, K.-J., Chapelle, D., Lee, P.S.: A shell problem highly sensitive to thickness changes. Int. J. Numer. Meth. Eng. **57**, 1039–1052 (2003)
24. Farin, G.: Curve and Surfaces for Computer Aided Geometric Design, A Practical Guide, 5th edn. Morgan Kaufmann Publishers, Los Altos (1999)
25. Gregory, J.A.: Smooth interpolation without twist constraint. Computer Aided Geometric Design. R.E. Barnhill and R. F. Riesenfeld, Academic Press, New York (1974)
26. Areias, P.M.A., Song, J.-H., Belytschko, T.: A finite-strain quadrilateral shell element based on discrete Kirchhoff–Love constraints. Int. J. Numer. Methods Eng. **64**(9), 1166–1206 (2005)
27. Greco, L., Cuomo, M.: B-spline interpolation for Kirchhoff-Love space rod. Comput. Methods Appl. Mech. Eng. **256**, 251–269 (2013)
28. Greco, L., Cuomo, M.: An implicit g^1 multi patch B-spline interpolation for Kirchhoff–Love space rod. Comput. Methods Appl. Mech. Eng. **269**, 173–197 (2014)
29. Greco, L., Cuomo, M.: An isogeometric implicit g^1 mixed finite element for Kirchhoff space rods. Comput. Methods Appl. Mech. Eng. **298**, 325–349 (2016)
30. Ciancio, D., Carol, I., Cuomo, M.: On inter-element forces in the FEM-displacement formulation, and implications for stress recovery. Int. J. Numer. Methods Eng. **66**(3), 502–528 (2006)
31. Ciancio, D., Carol, I., Cuomo, M.: Crack opening conditions at 'corner nodes' in FE analysis with cracking along mesh lines. Eng. Fract. Mech. **74**(13), 1963–1982 (2007)
32. Green, A.E., Zerna, W.: Theoretical Elasticity. Oxford University Press, Oxford (1954)
33. Chapelle, D., Bathe, K.-J.: The Finite Element Analysis of Shells-Fundamentals, 2nd edn. Springer, Berlin (2011)
34. Pietraszkiewicz, W.: Lagrangian description and incremental formulation in the non-linear theory of thin shell. Int. J. Non-Linear Mech. **19**(2), 115–140 (1984)
35. Eremeyev, V.A., Pietraszkiewicz, W.: The non linear theory of elastic shells with phase transition. J. Elast. **74**(1), 67–86 (2004)
36. Placidi, L., Andreaus, U., Della Corte, A., Lekszyck, T.: Gedanken experiments for the determination of two-dimensional linear second gradient elasticity coefficients. Zeitschrift für Angew. Math. und Phys. **66**(6), 3699–3725 (2015)
37. dell'Isola, F., Seppecher, P., Madeo, A.: How contact interactions may depend on the shape of cauchy cuts in n-th gradient continua: approach á la D'Alembert. ZAMP **63**, 1119–1141 (2012)
38. Auffray, N., dell'Isola, F., Eremeyev, V., Madeo, A., Rosi, G.: Analytical continuum mechanics á la Hamilton–Piola: least action principle for second gradient continua and capillary fluids. Math. Mech. Solids **20**(4), 375–417 (2015)
39. Coons, S.: Surface for computer aided design of space forms. Project MAC-TR 41. Technical report, MIT (1967)
40. Farin, G., Hansford, D.: Agnostic G1 Gregory surfaces. Graph. Models **74**(6), 346–350 (2012)
41. Barsky, B.A., DeRose, T.D.: Geometric continuity of parametric curves: three equivalent characterizations. IEEE Comput. Gr. Appl. **9**(6), 60–68 (1989)
42. Greco, L., Cuomo, M., Contrafatto, L., Gazzo, S.: An efficient blended mixed B-spline formulation for removing membrane locking in plane curved Kirchhoff rods. Comput. Methods Appl. Mech. Eng. **324**, 476–511 (2017)
43. Greco, L., Cuomo, M., Contrafatto, L.: A reconstructed local $\bar{B}$ formulation for isogeometric Kirchhoff–Love shells. Comput. Methods Appl. Mech. Eng. **332**, 462–487 (2018)
44. Cuomo, M.: Continuum model of microstructure induced softening for strain gradient materials. Math. Mech. Solids (2018). https://doi.org/10.1177/1081286518755845
45. Quang, Wang, Da-ju, Wang: Singularity under a concentrated force in elasticity. Appl. Math. Mech. **14**(8), 707–711 (1993)
46. dell'Isola, F., Corte, A.D., Giorgio, I.: Higher-gradient continua: the legacy of Piola, Mindlin, Sedov and Toupin and some future research perspectives. Math. Mech. Solids **22**(4), 852–872 (2017)
47. Boutin, C., dell'Isola, F., Giorgio, I., Placidi, L.: Linear pantographic sheets: asymptotic micro-macro models identification. Math. Mech. Complex Syst. **5**(2), 127–162 (2017)
48. Giorgio, I., Rizzi, N.L., Turco, E.: Continuum modelling of pantographic sheets for out-of-plane bifurcation and vibrational analysis. Proc. R. Soc. Lond. A **473**(2207), 21 (2017)
49. Steigmann, D.J., dell'Isola, F.: Mechanical response of fabric sheets to three-dimensional bending, twisting, and stretching. Acta Meccanica Sinica **31**(3), 373–382 (2015)
50. Giorgio, I., Della Corte, A., dell'Isola, F., Steigmann, D.J.: Buckling modes in pantographic lattices. Comptes Rendus - Mécanique **344**, 487–501 (2016)

51. Misra, A., Lekszycki, T., Giorgio, I., Ganzosch, G., Wolfgang, H.M., dell'Isola, F.: Pantographic metamaterials show atypical poynting effect reversal. Mech. Res. Commun. **89**, 6–10 (2018)
52. Turco, E., Giorgio, I., Misra, A., dell'Isola, F.: King post truss as a motif for internal structure of (meta)material with controlled elastic properties. R. Soc. Open Sci. **4**(10), 171153 (2017)

Publisher's Note Springer Nature remains neutral with regard to jurisdictional claims in published maps and institutional affiliations.